

A non-staggered, conservative, $\nabla \cdot \vec{B} = 0$, finite-volume scheme for 3D implicit extended magnetohydrodynamics in curvilinear geometries

L. Chacón

Theoretical Division, Los Alamos National Laboratory, Los Alamos, NM 87545, USA

Received 19 June 2004

Available online 18 October 2004

Abstract

In the development of spatial difference schemes for magnetohydrodynamics (MHD), the preservation of continuum properties such as conservation of mass, momentum, and energy, as well as required electromagnetic constraints ($\nabla \cdot \vec{B} = \nabla \cdot \vec{j} = 0$, where $\vec{j} = \nabla \times \vec{B}$ is the electrical current), is desirable to preserve numerical accuracy. Moreover, simplicity of the scheme is also a desirable feature, particularly when an *implicit* implementation is considered (the focus of this paper). We propose here a finite-volume, cell-centered (non-staggered) scheme for the extended MHD formulation that: (1) is suitable for *implicit* implementations in arbitrary curvilinear geometries, (2) is conservative, (3) preserves both the magnetic field and the electrical current solenoidal to machine precision, and (4) is linearly and nonlinearly stable in the absence of numerical and physical dissipation. Crucial to the viability of the scheme is the use of a clever interpolation scheme (ZIP [Hirt, J. Comput. Phys. 2 (1968) 339–355]), the proper treatment of boundary conditions in curvilinear geometry, and a novel treatment of geometric source terms in the momentum equation that ensures their exact cancellation in the absence of pressure forces.

© 2004 Elsevier B.V. All rights reserved.

PACS: 02.60.Cb; 02.60.Jh; 02.70.Fj; 52.30.-q; 52.65.Kj

Keywords: Implicit MHD; Newton–Krylov solvers; Finite volumes; Non-staggered solenoidal schemes; Conservative schemes; Curvilinear geometries

1. Introduction

When considering a discrete spatial representation of the magnetohydrodynamics (MHD) equations, the preservation of continuum properties such as conservation of mass, momentum, and energy, as well as required electro-

E-mail address: chacon@lanl.gov (L. Chacón).

magnetic constraints ($\nabla \cdot \vec{B} = \nabla \cdot \vec{j} = 0$, where $\vec{j} = \nabla \times \vec{B}$ is the electrical current), is desirable to avoid spurious unphysical modes and preserve numerical accuracy. Conservation has been a major focus of the explicit, shock-capturing ideal MHD community, since it is well known that these properties are essential to numerically produce the correct Rankine–Hugoniot jump conditions in shock waves [2]. Also, the preservation of the solenoidal property of the magnetic field numerically is essential if the conservative form of the momentum equation is to be used, or otherwise unphysical parallel (to the magnetic field) body forces result [3].

In the implicit MHD community, however, conservation has not been regarded as essential, as evidenced by the significant number of efforts that consider the non-conservative form of the MHD equations [4–8]. In transient implicit calculations, the focus is not on advection- or shock-dominated regimes, but rather on the study of long-time-scale, low-frequency phenomena, whose time scales are much longer than those of typical MHD wave phenomena. Explicit techniques are very inefficient for this purpose due to numerical CFL constraints, and therefore an implicit approach is desirable. In addition, due to the long time spans of interest, transport physics cannot be neglected in the MHD model. In fact, fundamental long-term dynamical processes (compared to typical frequencies of MHD wave phenomena) such as magnetic reconnection and resistive instabilities (tearing modes) require dissipation to occur. Therefore, these plasmas are best described by the extended MHD formulation, which includes—among others—the effects of transport.

Numerical simulation of long time-scale dynamics requires one to accurately follow the solution for very long time spans. Since conservation and $\nabla \cdot \vec{B} = \nabla \cdot \vec{j} = 0$ are fundamental properties of the MHD model, we argue that their preservation is essential to ensure accuracy of such simulations. Otherwise, numerical conservation errors may grow uncontrolled, casting doubt on the predictive capability of the numerical scheme. Therefore, for a given nominal order of accuracy, we regard a conservative scheme as possessing a higher standard of accuracy than a non-conservative scheme. (We point out that some authors in the implicit MHD community justify using a non-conservative scheme as a means to avoid numerical noise [5]. In what follows, we will discuss the source of noise and how to avoid it in conservative formulations.)

Within the finite-volume approach, solenoidal, conservative schemes have been achieved traditionally using so-called staggered formulations, in which thermodynamic scalars and vector components live in different locations within a finite-volume cell (usually scalars live at cell centers, whereas vector components live either at cell faces or at cell vertices). Staggered formulations have been shown to be adequate for most fluid applications owing to their robustness and stability. In addition, they may possess “mimetic” properties if implemented correctly (by mimetic we mean that integro-differential properties of the differential operators in the continuum are satisfied also in the discrete [9]). In the context of explicit, shock-capturing methods for ideal MHD, most authors have used staggered approaches as the basis for a finite-volume discretization (see, for instance, Refs. [10–14]; an excellent review and comparison of several of these approaches can be found in Ref. [15]). Some implicit MHD efforts [6,7] have also employed staggered schemes as the basis for their spatial discretization.

Staggered schemes, however, are cumbersome to implement and maintain, even more so when combined with adaptive gridding techniques [such as adaptive mesh refinement (AMR)] and/or domain decomposition for parallel applications. From this perspective, (non-staggered) cell-centered finite-volume discretizations are preferred. This is particularly the case for implicit MHD applications, where the necessity of performing global matrix inversions makes the simplified bookkeeping of cell-centered approaches a major advantage. In fact, while there have been recent serious efforts in the *explicit* shock-capturing community to produce viable non-staggered schemes [15], cell-centered regimes have been the focus of implicit schemes for quite some time [4,5,16,17]. However, as mentioned earlier, many of these efforts for implicit MHD are not conservative [4–8], and most do not preserve $\nabla \cdot \vec{B} = 0$ (with the notable exceptions of Refs. [6,7]). In addition, they feature fairly dissipative first-order semi-implicit temporal schemes, and some even require additional dissipation to deal with numerical antidiffusive modes [5].

In the present study, we propose a new cell-centered spatial scheme suitable for an *implicit* treatment of the MHD equations that is both conservative and solenoidal to machine precision. The scheme is non-dissipative, suitable for arbitrary curvilinear (non-orthogonal) geometries, and stable to linear (red-black) and nonlinear (antidiffusion) numerical modes, even in the absence of physical/numerical dissipation. The spatial scheme is independent

of the temporal discretization details, and is therefore compatible with high-order, fully-implicit time-stepping techniques. We test the spatial scheme using an implicit, second-order Crank–Nicolson temporal scheme, and we employ Newton–Krylov methods for the required algebraic inversions. We demonstrate theoretically (Appendix C) and numerically (Section 5) that Newton–Krylov solvers are ideally suited to deal with the associated nonlinear systems because they preserve the conservation properties of the scheme for arbitrary nonlinear tolerances. This property avoids “oversolving” the nonlinear system to machine accuracy for the sake of conservation, making the implementation very efficient.

A fundamental concern of this study is the demonstration of the adequacy of the scheme for generalized curvilinear geometries. The effort is justified in that this is a fundamental requirement, for instance, in the treatment of realistic geometries of magnetic fusion devices. A crucial property of the scheme is that its conservation properties (except for the momentum equation; see Section 3) are essentially unaffected when considering generalized curvilinear geometries. The present study generalizes work in Refs. [5,16], where general *orthogonal* geometries were considered in the context of non-staggered finite-difference schemes.

We re-emphasize that an implicit treatment is of interest to study transient physical regimes where shocks are absent, and dynamical time scales are very long compared to typical MHD wave phenomena time scales. (We note that an implicit treatment may be of interest in shock-dominated regimes for the purpose of finding steady-state solutions.) In fact, if shocks—or otherwise very fast moving features—are present in the solution, an implicit treatment presents little advantage with respect to a standard explicit approach, and therefore the latter is preferable for its simplicity [17]. In this light, it is clear that strictly monotonic difference schemes are not an essential feature of implicit schemes (although there are some efforts [17,18] that have adapted approximate Riemann solvers for an implicit treatment). In this study, we employ a variation of central difference schemes called ZIP [1], which possesses remarkable properties, including nonlinear stability, exact conservation, second-order accuracy, and mimicking the chain rule of derivatives numerically. We recognize, however, that monotonicity may nevertheless be a useful feature for the robustness of any spatial scheme, and we leave for future work the merging of ZIP with a flexible, monotonic advection algorithm such as SMART [19].

The remainder of the paper is organized as follows. Section 2 introduces the MHD model of choice and suitable normalizations. Section 3 presents the complete formulation for a general curvilinear representation of the MHD equations. The spatial discretization details (including the details of ZIP) are presented in Section 4. Numerical tests demonstrating the advertised properties of the scheme are presented in Section 5. Finally, we conclude in Section 6.

2. Model equations

We consider the compressible resistive MHD model, given by:

$$\text{Continuity: } \frac{\partial \rho}{\partial t} + \nabla \cdot (\rho \vec{v} - D \nabla \rho) = 0, \quad (1)$$

$$\text{Faraday's law: } \frac{\partial \vec{B}}{\partial t} + \nabla \times \vec{E} = 0; \quad \vec{E} = -\vec{v} \times \vec{B} + \eta(T) \vec{j}; \quad \vec{j} = \frac{1}{\mu_0} \nabla \times \vec{B}, \quad (2)$$

$$\text{Momentum: } \frac{\partial(\rho \vec{v})}{\partial t} + \nabla \cdot \left[\rho \vec{v} \vec{v} - \frac{\vec{B} \vec{B}}{\mu_0} + \vec{T} \left(p + \frac{B^2}{2\mu_0} \right) - \rho \nu(T) \nabla \vec{v} \right] = 0, \quad (3)$$

$$\text{Energy: } \frac{\partial T}{\partial t} + \vec{v} \cdot \nabla T + (\gamma - 1) T \nabla \cdot \vec{v} = 0, \quad (4)$$

where the plasma is assumed polytropic $p \propto n^\gamma$, with γ the polytropic constant, $p = (n_i + n_e)T = 2nT$ the pressure, $T = T_i = T_e$ the ion/electron temperature, and $n = n_i = n_e$ the ion/electron density. In these equations, $\rho = m_i n$ is the ion mass density, \vec{v} is the plasma velocity, \vec{B} is the magnetic field, $\eta(T)$ is the resistivity, $\nu(T)$

is the kinematic viscosity, and D is a particle diffusivity that models cross-field particle diffusion. (Such particle diffusivity D is not self-consistently considered in Eq. (3), and hence should be regarded as *ad-hoc* in nature.)

The energy $E = \rho v^2/2 + B^2/2\mu_0 + p/(\gamma - 1)$ is not conserved in this model, since heat sources such as Joule heating (ηj^2) and viscous heating ($\rho v(\nabla \vec{v})^T : \nabla \vec{v}$) are not included in the temperature equation. Proper consideration of these terms is left for future work. However, for the sake of completeness, we state the temperature equation supplemented with dissipation heat sources $Q = \eta j^2 + \rho v(\nabla \vec{v})^T : \nabla \vec{v}$, and heat flux \vec{q} :

$$\frac{\partial T}{\partial t} + \vec{v} \cdot \nabla T + (\gamma - 1) \left[T \nabla \cdot \vec{v} + \frac{\nabla \cdot \vec{q} - Q}{2n} \right] = 0.$$

Alternatively to the temperature equation, one can use the energy equation,

$$\frac{\partial E}{\partial t} + \nabla \cdot \left[\vec{v} \left(\rho \frac{v^2}{2} + \frac{\gamma p}{\gamma - 1} \right) + \vec{E} \times \vec{B} - \rho v \nabla \frac{v^2}{2} + \vec{q} \right] = 0. \quad (5)$$

The temperature equation is advantageous when the heat flux \vec{q} is a strong function of the temperature, as in fusion applications. The energy equation is advantageous when exact conservation of energy is critical (with the proposed spatial scheme and the proper source terms, the temperature formulation conserves energy only up to truncation error).

In Alfvénic units (i.e. Alfvén speed $v_A = B_0/\sqrt{\mu_0 \rho_0}$, Alfvén time $\tau_A = L/v_A$, where B_0 , ρ_0 , and L are the reference magnetic field, density, and length, respectively), the dimensionless form of the set of equations above reads:

$$\frac{\partial \rho}{\partial t} + \nabla \cdot (\rho \vec{v} - D \nabla \rho) = 0, \quad (6)$$

$$\frac{\partial \vec{B}}{\partial t} + \nabla \times \vec{E} = 0; \quad \vec{E} = -\vec{v} \times \vec{B} + \eta(T) \vec{j}; \quad \vec{j} = \nabla \times \vec{B}, \quad (7)$$

$$\frac{\partial (\rho \vec{v})}{\partial t} + \nabla \cdot \left[\rho \vec{v} \vec{v} - \vec{B} \vec{B} - \rho v(T) \nabla \vec{v} + \vec{T} \left(p + \frac{B^2}{2} \right) \right] = 0, \quad (8)$$

$$\frac{\partial T}{\partial t} + \vec{v} \cdot \nabla T + (\gamma - 1) T \nabla \cdot \vec{v} = 0, \quad (9)$$

and $p = 2\rho T$. At this point all quantities are dimensionless, and D , η , v are the reciprocals of the particle diffusivity, the Lundquist number, and the Reynolds number, respectively.

3. Generalized curvilinear formulation

Consider the general mapping $\vec{x} = \vec{x}(\vec{\xi})$ from the logical ($\vec{\xi}$) to the physical (\vec{x}) space. We associate to this mapping normal ($\vec{i} = \nabla \xi_i$) and tangential ($\vec{i}_j = \frac{1}{J} \frac{\partial \vec{x}}{\partial \xi_j} = \nabla \xi_j \times \nabla \xi_k$) vector bases, satisfying the orthogonality property $\vec{i} \cdot \vec{k}_k = \delta_k^i J^{-1}$, with J the Jacobian of the transformation $\vec{x} = \vec{x}(\vec{\xi})$, and δ_k^i the Kronecker delta. A given vector field \vec{A} has covariant components $A_i = J \vec{A} \cdot \vec{i}_i$, and contravariant components $A^i = J \vec{A} \cdot \vec{i}$. These are related to each other by the contravariant metric tensor $g^{ik} = \vec{i} \cdot \vec{k}$ as $A^i = g^{ik} A_k$, and by the covariant metric tensor $g_{ik} = J \vec{i}_i \cdot \vec{k}_k$ as $A_i = g_{ik} A^k$. The covariant and contravariant metric tensors are related by $g_{in} g^{nk} = \delta_i^k$.

We note that our definition of normal and tangential vectors differs from the standard definition [20] by the reciprocal Jacobian factor in \vec{i}_j (the standard curvilinear representation employs $\nabla \xi_i$ as normal vectors and $\frac{\partial \vec{x}}{\partial \xi_j}$ as tangential vectors, which satisfy the orthogonality property $\nabla \xi_i \cdot \frac{\partial \vec{x}}{\partial \xi_j} = \delta_j^i$). However, with our definition, the normal vectors are irrotational ($\nabla \times \vec{i} = \vec{0}$) and the tangential vectors are solenoidal ($\nabla \cdot \vec{i}_j = 0$), which provides ideally suited bases for projecting conservation laws onto the logical representation. In particular, Jacobian factors

J are naturally absorbed in the contravariant vector components, making the discretization more transparent. For the reader familiar with the standard formulation, all the equations presented below can be readily transformed by replacing $A^i \rightarrow JA^i$, $g^{ij} \rightarrow Jg^{ij}$, and $g_{ij} \rightarrow g_{ij}/J$.

In terms of these components, and assuming the Jacobian of the mapping does not change in time (e.g., $\partial_t J = 0$, except for instantaneous, infrequent changes in resolution, such as in AMR schemes), the MHD equations (6)–(9) can be expressed in the logical space as:

$$\partial_t(J\rho) + \partial_i(\rho v^i) - \partial_i(Dg^{in}\partial_n\rho) = 0, \quad (10)$$

$$\partial_t B^i + \epsilon_{ink}\partial_n E_k = 0, \quad (11)$$

$$\partial_t(\rho v^i) + \partial_n(J^{-1}T^{ni}) + J^{-1}T^{nk}\Gamma_{nk}^i = 0, \quad (12)$$

$$\partial_t(JT) + v^i\partial_i T + (\gamma - 1)T\partial_i v^i = 0. \quad (13)$$

Here, $\partial_i \equiv \partial/\partial\xi_i$, $\partial_t \equiv \partial/\partial t$, $\nabla \equiv \partial/\partial\vec{x}$, $\Gamma_{nk}^i = -(\nabla\nabla\xi_i)_{nk} = -J^2\vec{n} \cdot (\nabla\nabla\xi_i) \cdot \vec{k} = \frac{\partial^2\vec{x}}{\partial\xi_k\partial\xi_n} \cdot \nabla\xi_i$ is the Christoffel symbol of the second kind [20], and:

$$E_i = J^{-1}\epsilon_{ink}v^n B^k - \eta j_i,$$

$$T^{ki} = \rho v^i v^k - B^i B^k + g^{ik}(Jp + B_n B^n/2) - \rho v[\nabla\vec{v}]^{ki}.$$

Here, the contravariant tensor components $[\nabla\vec{v}]^{ki}$ are given by (Appendix A):

$$[\nabla\vec{v}]^{ki} = J^2\vec{k} \cdot (\nabla\vec{v}) \cdot \vec{i} = g^{kl}(\partial_l v^i - v^l \Gamma_{ln}^i + v^n \Gamma_{nl}^i). \quad (14)$$

Note that, in the logical representation, a geometric source $J^{-1}T^{nk}\Gamma_{nk}^i$ is present. This source corresponds to Coriolis (inertial) forces as fluid elements traverse a curved space. It is not numerical but geometric in nature, unavoidable except in flat (Cartesian) space, and independent of the discretization of choice (the equations are still expressed in the continuum at this point). The presence of the Coriolis terms may prevent exact numerical conservation of the momentum, and require a careful numerical treatment to minimize their impact (Section 4.4.3).

It is worth noting at this point that one can take the derivative of the Jacobian analytically [20] to find $\partial_n J = J\Gamma_{nk}^k$, and hence the momentum equation can be rewritten as:

$$\partial_t(J\rho v^i) + \partial_n T^{ni} - T^{ni}\Gamma_{nk}^k + T^{nk}\Gamma_{nk}^i = 0. \quad (15)$$

This alternative formulation avoids J^{-1} , and hence is advantageous for coordinates systems in which the Jacobian vanishes at a singular point (e.g., cylindrical, toroidal, spherical, at $r = 0$). In fact, in particular coordinate systems and for selected velocity components (e.g., v_ϕ in cylindrical coordinates), Eq. (15) may be interpreted as the conservation of angular momentum.

The time-independence assumption of the mapping implies that the formulation in Eqs. (10)–(13) is not suitable for the use of r -refinement (moving mesh) adaptive techniques [although it is suitable for AMR techniques (h -refinement), where changes in resolution are instantaneous]. While the derivation of the MHD equations for time-dependent mappings is out of the scope of this work, we point out that, as described in [20], time-dependent mappings only result in small modifications to Eqs. (10)–(13): they can still be cast in conservative form but including a “node velocity” in advection terms. Therefore, the discussion below can be generalized straightforwardly to time-dependent mappings, and the time-independence assumption of the mapping should not be regarded as a fundamental limitation of the study.

4. Spatial discretization

In a non-staggered spatial representation, all quantities are known at cell centers (see Fig. 1). Such a representation is desirable because it substantially simplifies the development and maintenance of implicit, parallel, adaptive

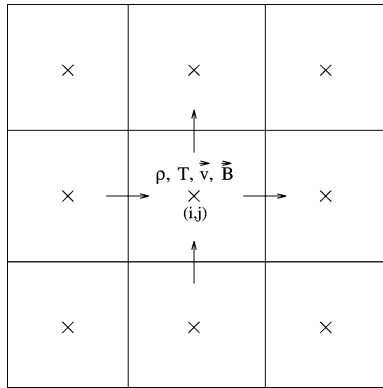


Fig. 1. Schematic of a cell-centered grid representation on a 2D grid. All quantities are known at the cell centers. Fluxes at faces need to be interpolated.

algorithms. Recently, in the context of explicit, shock-capturing schemes, Tóth [15] demonstrated that staggered schemes commonly employed in MHD can in fact be reduced to cell-centered finite volume schemes with suitably defined fluxes at faces. He compared the accuracy performance of staggered and cell-centered formulations and found no advantage of the former over the latter. However, the ideas in Ref. [15] are fundamentally based on time upwinding using local explicit Riemann problems (which provide the required coupling to avoid the well-known checkerboard instability of cell-centered representations), and hence cannot be readily extended to implicit schemes.

We are therefore motivated here to develop a cell-centered, finite volume discretization suitable for an implicit integration of Eqs. (6)–(9) in a general curvilinear geometry. We focus on structured and logically rectangular grids. The scheme will not be shock-capturing, but this is not viewed as a fundamental limitation, since implicit methods are not well suited for transiently modeling such physics [17]. Without loss of generality, we demonstrate the main properties of the scheme in 2D geometry. Extension to 3D is straightforward.

Equations are discretized on the logical grid (ξ), which remains uniform and logically rectangular at all times. In the logical representation, equations remain Cartesian-like except for sources. Since all quantities are defined at cell centers, interpolation is needed to find fluxes at cell faces and provide local conservation. The choice of interpolation is crucial and determines the properties of the spatial scheme.

Two main ingredients are key for the proposed approach to attain the advertised properties (namely, conservation, solenoidal magnetic field and electrical current, linear and nonlinear stability in the absence of dissipation): (1) the so-called ZIP interpolation [1] to find fluxes at faces from cell-centered quantities, and (2) a proper treatment of the boundary conditions. These are described in the next sections.

4.1. The ZIP average

The ZIP average [1] avoids certain nonlinear instabilities that appear in cell-centered grids as a result of poorly devised cell-to-face interpolations. We demonstrate the concept in 1D Cartesian geometry, with a nonlinear advection equation $\partial_t \Phi + \partial_x(v\Phi) = 0$. Both v and Φ are cell-centered quantities that have non-trivial spatial and temporal dependence. A finite-volume discretization at the cell i yields:

$$\partial_x(v\Phi)_i = \frac{(v\Phi)_{i+1/2} - (v\Phi)_{i-1/2}}{h} + \mathcal{O}(h^2). \quad (16)$$

In principle, there is freedom to choose an appropriate interpolation from the cell centers $(i-1, i, i+1)$ to the faces $(i-1/2, i+1/2)$. We consider here two second-order accurate choices (see [1] for a similar analysis and

conclusion for other common choices):

$$\text{Flux average (FA): } (v\Phi)_{i+1/2} = \frac{1}{2}[(v\Phi)_{i+1} + (v\Phi)_i] + \mathcal{O}(h^2),$$

$$\text{ZIP: } (v\Phi)_{i+1/2} = \frac{1}{2}[v_i\Phi_{i+1} + v_{i+1}\Phi_i] + \mathcal{O}(h^2).$$

Introducing these interpolations in the spatial derivative in Eq. (16), we find:

$$\text{FA: } \frac{(v\Phi)_{i+1/2} - (v\Phi)_{i-1/2}}{h} = \frac{(v\Phi)_{i+1} - (v\Phi)_{i-1}}{2h},$$

$$\text{ZIP: } \frac{(v\Phi)_{i+1/2} - (v\Phi)_{i-1/2}}{h} = v_i \frac{\Phi_{i+1} - \Phi_{i-1}}{2h} + \Phi_i \frac{v_{i+1} - v_{i-1}}{2h}.$$

We note that the ZIP differencing satisfies the chain rule of derivatives in discrete form *while being exactly conservative* (since Eq. (16) is in flux form). Moreover, Hirt demonstrated [1] that FA is nonlinearly unstable (in the form of anti-diffusion) while ZIP is not. This is easily seen from a Taylor expansion of the discrete equations about x_i to obtain the so-called modified equation (ME):

$$\text{FA: } \frac{(v\Phi)_{i+1} - (v\Phi)_{i-1}}{2h} \approx (v\Phi)' + \frac{h^2}{2}(\Phi'v'' + \underline{v'\Phi''} + \frac{1}{3}[\Phi v''' + v\Phi''']),$$

$$\text{ZIP: } v_i \frac{\Phi_{i+1} - \Phi_{i-1}}{2h} + \Phi_i \frac{v_{i+1} - v_{i-1}}{2h} \approx (v\Phi)' + \frac{h^2}{6}(\Phi v''' + v\Phi'''),$$

where the prime indicates a derivative with respect to x . The ME is the actual evolution equation for Φ . Clearly, FA has a potentially anti-diffusive term for Φ in its ME (underlined term) since the coefficient v' can take an arbitrary sign, while ZIP does not. This antidiffusive term is the source of *nonlinear* instabilities, and can only be cured by offsetting the negative diffusion coefficient by means of additional dissipation [5].

This result also sheds some light on the better performance of non-conservative schemes in regards to numerical noise. In particular, for non-conservative schemes, FA and ZIP are equivalent, and none have antidiffusive terms in their ME. This explains why many authors have favored non-conservative cell-centered schemes for implicit applications [4–8] as a means to obtain cleaner solutions. With the use of ZIP, however, a fully conservative approach is possible while avoiding the numerical pollution resulting from antidiffusive terms.

In the previous discussion, temporal discretization errors have been neglected. This is justified by several reasons: (1) in fully implicit schemes, temporal and spatial truncation errors are decoupled [21], and hence their effects can be studied independently; (2) most implicit schemes are linearly A-stable for arbitrary time steps, and therefore the only uncertainty is nonlinear instabilities stemming from spatial truncation errors; and (3) the leading-order truncation error terms of second-order temporal schemes (the choice here) are dispersive in nature, and hence cannot offset the antidiffusion terms present in the spatial truncation error of the FA scheme. This is also true for higher-order temporal schemes, where dissipative contributions to the truncation error are much too small to offset antidiffusion terms of order $\mathcal{O}(h^2)$.

Summarizing, the ZIP average features the following properties: (1) it is exactly conservative, (2) satisfies the chain rule numerically (the importance of this will be apparent shortly), (3) it is nonlinearly stable, and (4) precludes the growth of red-black modes since coupling to the cell values of the quantities of interest is provided (i.e. both v_i and Φ_i appear in the discrete approximation). In the following, we briefly describe how this is applied to the MHD system.

4.2. Discretization of the density equation

The density (continuity) equation is of the form of a scalar advection-diffusion equation. The discretization of the advection part follows straightforwardly from the previous example, which can be generalized readily to multiple dimensions.

Regarding the diffusion term, and as is clear from Eq. (10), the discretization of the Laplacian operator in generalized non-orthogonal coordinates results in a tensor-diffusion operator $\partial_i(g^{ij}\partial_j\rho)$, where g^{ij} is the symmetric positive definite (SPD) contravariant metric tensor. A proper discretization of the diffusion term on the logical grid should preserve the SPD property.

Formally, the discretization of the Laplacian operator in a non-orthogonal representation is identical to the discretization of a diffusion problem in Cartesian coordinates with an SPD tensor-valued diffusion coefficient \vec{D} , $\nabla \cdot (\vec{D} \cdot \nabla \Phi)$. We employ the following second order, SPD discrete approximation to the tensor-diffusion operator:

$$\begin{aligned} [\nabla \cdot (\vec{D} \cdot \nabla \Phi)]_{i,j} \approx & \frac{1}{h_{x,i}} \left[D_{xx}|_{i+1/2,j} \frac{\Phi_{i+1,j} - \Phi_{i,j}}{h_{x,i+1/2}} - D_{xx}|_{i-1/2,j} \frac{\Phi_{i,j} - \Phi_{i-1,j}}{h_{x,i-1/2}} \right] \\ & + \frac{1}{h_{y,j}} \left[D_{yy}|_{i,j+1/2} \frac{\Phi_{i,j+1} - \Phi_{i,j}}{h_{y,j+1/2}} - D_{yy}|_{i,j-1/2} \frac{\Phi_{i,j} - \Phi_{i,j-1}}{h_{y,j-1/2}} \right] \\ & + \frac{1}{2h_{x,i}h_{y,j}} \left[D_{xy}|_{i+1/2,j+1/2} (\Phi_{i+1,j+1} - \Phi_{i,j}) + D_{xy}|_{i-1/2,j-1/2} (\Phi_{i-1,j-1} - \Phi_{i,j}) \right. \\ & \left. - D_{xy}|_{i+1/2,j-1/2} (\Phi_{i+1,j-1} - \Phi_{i,j}) - D_{xy}|_{i-1/2,j+1/2} (\Phi_{i-1,j+1} - \Phi_{i,j}) \right], \end{aligned}$$

where $h_{x,i}$ and $h_{y,j}$ are the grid spacings at the node (i, j) , and $h_{x,i+1/2} = (h_{x,i+1} + h_{x,i})/2$ (and similarly for $h_{y,j+1/2}$). Extension to three dimensions is straightforward.

4.3. Discretization of the temperature equation

For its discretization, the advective term in the temperature equation (9) is rewritten in a conservative form as:

$$\frac{\partial T}{\partial t} + \nabla \cdot (\vec{v}T) + (\gamma - 2)T\nabla \cdot \vec{v} = 0. \quad (17)$$

Due to the chain-rule property of ZIP, the discrete forms of Eqs. (9) and (17) are numerically identical within the domain, and only differ at boundaries. However, this form is more consistent with the approach employed here to impose boundary conditions (Section 4.6), and results in less numerical noise generated at boundaries. The conservative advection term in Eq. (17) is then trivially discretized using ZIP as explained above.

4.4. Discretization of the momentum equation (EOM)

In the discretization of the momentum equation, there are three different aspects that should be addressed separately: (1) the treatment of the ideal terms, (2) the treatment of viscous terms, and (3) the treatment of the geometric sources (Coriolis forces). We proceed to discuss each of these in the next subsections.

4.4.1. Discretization of ideal terms in EOM

For the ideal terms, we employ ZIP. We illustrate the concept using a single component of the momentum $\rho\vec{v}$, omitting geometric sources and viscous terms (discussed later):

$$\frac{\partial(\rho v^k)}{\partial t} + \partial_m \left[\frac{1}{J} \left(\rho v^k v^m - B^k B^m + g^{km} \left(Jp + \frac{B_l B^l}{2} \right) \right) \right].$$

All terms within the square brackets are at least quadratically nonlinear (since $p = 2\rho T$), and hence ZIP differencing can be applied straightforwardly. For instance, the ZIP interpolation at the $(i, j + 1/2)$ face for the ideal terms gives:

$$\begin{aligned} (J^{-1} \rho v^k v^m)_{i,j+1/2} & \approx \frac{1}{4} J_{i,j+1/2}^{-1} [(\rho v^m)_{i,j+1} v_{i,j}^k + (\rho v^k)_{i,j} v_{i,j+1}^m + (\rho v^k)_{i,j+1} v_{i,j}^m + (\rho v^m)_{i,j} v_{i,j+1}^k], \\ (J^{-1} B^k B^m)_{i,j+1/2} & \approx \frac{1}{2} J_{i,j+1/2}^{-1} [B_{i,j+1}^k B_{i,j}^m + B_{i,j}^k B_{i,j+1}^m], \end{aligned}$$

$$(J^{-1}g^{km}B_lB^l)_{i,j+1/2} \approx \frac{1}{2}(J^{-1}g^{km})_{i,j+1/2}[B_{li,j+1}B_{i,j}^l + B_{li,j}B_{i,j+1}^l],$$

$$(g^{km}p)_{i,j+1/2} \approx g_{i,j+1/2}^{km}[\rho_{i,j+1}T_{i,j} + \rho_{i,j}T_{i,j+1}],$$

where (i, j) sample the grid nodes and (k, m, l) sample the vector components. Note that the triple-product term has been “symmetrized” to avoid skewness in the discretization.

4.4.2. Discretization of viscous terms in EOM

The numerical approximation of the viscous terms in the EOM requires one to discretize terms of the form:

$$\partial_k(J^{-1}\rho v[\nabla\vec{v}]^{km}) = \partial_k\left(\rho v\frac{g^{kl}}{J}[\partial_l v^m - v^m\Gamma_{ln}^n + v^n\Gamma_{nl}^m]\right).$$

This is done using a standard finite-volume approximation, with fluxes at faces defined so as to provide a compact discretization (i.e. which employs nearest neighbors only). We exemplify the approach by taking $k = 1$ and calculating fluxes at the face $(i + 1/2, j)$ as follows:

$$\begin{aligned} & \left(\rho v\frac{g^{1l}}{J}[\partial_l v^m - v^m\Gamma_{ln}^n + v^n\Gamma_{nl}^m]\right)_{i+1/2,j} \\ &= \left(\rho v\frac{g^{1l}}{J}\right)_{i+1/2,j} [\partial_l v^m - v^m\Gamma_{ln}^n + v^n\Gamma_{nl}^m]_{i+1/2,j} \\ &\approx (\rho v)_{i+1/2,j} \left(\frac{g_{i+1,j}^{1l} + g_{i,j}^{1l}}{J_{i+1,j} + J_{i,j}}\right) \left[(\partial_l v^m)_{i+1/2,j} - \frac{(v^m\Gamma_{ln}^n)_{i+1,j} + (v^m\Gamma_{ln}^n)_{i,j}}{2} \right. \\ &\quad \left. + \frac{(v^n\Gamma_{nl}^m)_{i+1,j} + (v^n\Gamma_{nl}^m)_{i,j}}{2} \right]. \end{aligned}$$

Some of the choices in this discrete representation are somewhat arbitrary, and others may perform equally well. We note, however, that preserving the product $(v\Gamma)$ cell-centered [i.e. $(v\Gamma)_{i+1/2,j} \approx [(v\Gamma)_{i+1,j} + (v\Gamma)_{i,j}]/2$] is important to produce adequate behavior in singular coordinate systems, since it allows certain cancellations of geometric factors to take place near the singular point. The discretization of the derivative $(\partial_l v^m)_{i+1/2,j}$ is different depending on whether $l = k$ (with $k = 1$ in this specific example) or not:

$$(\partial_l v^m)_{i+1/2,j} \approx \begin{cases} \frac{v_{i+1,j}^m - v_{i,j}^m}{h_{1,i+1/2}}, & l = k, \\ \frac{(\partial_l v^m)_{i+1,j} + (\partial_l v^m)_{i,j}}{2}, & l \neq k. \end{cases}$$

In the case $l \neq k$, $(\partial_l v^m)_{i,j}$ is evaluated using central differences. The evaluation of the viscosity coefficient (ρv) at the face $i + 1/2$ is done using a harmonic average [22]:

$$(\rho v)_{i+1/2,j} = \frac{2(\rho v)_{i,j}(\rho v)_{i+1,j}}{(\rho v)_{i,j} + (\rho v)_{i+1,j}}.$$

4.4.3. Discretization of geometric terms in EOM: Coriolis force-balance condition

A fundamental property of any satisfactory discretization of the EOM is that no body force results for a constant total pressure $p_{\text{tot}} = p + B_l B^l / (2J) = \text{const}$. This property should in fact be true to machine accuracy (and not just to truncation error), since even small truncation errors may fundamentally alter the dynamics for such cases. In general curvilinear geometry, the Coriolis force-balance condition is obtained by setting $p = 1$ and $\vec{v} = \vec{B} = 0$ in the EOM, to obtain:

$$\partial_n(g^{in}) + g^{kl}\Gamma_{kl}^i = 0, \quad i = 1, 2, 3. \quad (18)$$

This identity can be readily checked by using the definitions in Section 3. However, in general, it does not carry over to the discrete unless care is taken. We will show next that, owing to the fact that in our scheme all quantities are cell-centered, a simple prescription can be found that extends Eq. (18) to the discrete.

By definition, the Christoffel symbol of the second kind Γ_{kl}^i is given by [20]:

$$\Gamma_{kl}^i = (\partial_{lk}^2 \vec{x}) \cdot \nabla \xi_i. \quad (19)$$

Using the definitions in Section 3, we find straightforwardly that:

$$\Gamma_{kl}^i = \partial_k [J \vec{l}] \cdot \vec{i} = -J \vec{l} \cdot \partial_k \vec{i}.$$

But $\vec{l} = g_{lm} \vec{m}$, and therefore:

$$\Gamma_{kl}^i = -J g_{lm} \vec{m} \cdot \partial_k \vec{i} = -g_{lm} \partial_k [J \vec{m} \cdot \vec{i}] + g_{lm} [\vec{m} \cdot \vec{i} \partial_k J + J \vec{i} \cdot \partial_k \vec{m}].$$

We now notice, since $\vec{m} = \nabla \xi_m$, that $\partial_k \vec{m} = J (\nabla \nabla \xi_m) \cdot \vec{k}$, and therefore (Section 3) $J \vec{i} \cdot \partial_k \vec{m} = -g^{ij} \Gamma_{jk}^m$. Hence, recalling that $g^{mi} = J \vec{m} \cdot \vec{i}$, $\partial_k J = J \Gamma_{kj}^j$, and $g_{lm} g^{mi} = \delta_l^i$, we finally find:

$$\Gamma_{kl}^i = -g_{lm} \partial_k g^{mi} + \delta_l^i \Gamma_{kj}^j - g_{lm} g^{ij} \Gamma_{jk}^m. \quad (20)$$

The relevance of this result is that Eq. (18) can be readily obtained by operating Eq. (20) with $\sum_{lk} g^{lk}$ and using the covariant and contravariant metric tensor relationship, $g_{lm} g^{mi} = \delta_l^i$. This makes Eq. (20) suitable for a discrete definition of Γ_{kl}^i that satisfies the force balance condition (Eq. (18)), since the metric tensor relationship holds also in the discrete (to machine accuracy) at every cell center. Of course, the numerical approximation of $\partial_k g^{mi}$ in Eq. (20) must be consistent with that employed to discretize $\partial_k (g^{mi} p)$ in the EOM (Section 4.4.1).

As stated, however, Eq. (20) defines Γ_{kl}^i implicitly, and a cell-wise 27×27 matrix inversion would be required in order to find its components at every cell center. This, which could be affordable for static grids, becomes too expensive for dynamically adaptive grids. A much better approach is to use Eq. (20) as a corrector step. In this fashion, we consider a predictor step in which we numerically find values of Γ_{kl}^i at every cell center using its standard definition in Eq. (19) [which we call $(\Gamma^*)_{kl}^i$], and then correct them using Eq. (20) as follows:

$$\Gamma_{kl}^i = -g_{lm} \partial_k g^{mi} + \delta_l^i (\Gamma^*)_{kj}^j - g_{lm} g^{ij} (\Gamma^*)_{jk}^m. \quad (21)$$

It is straightforward to show that this definition of Γ_{kl}^i still satisfies Eq. (18) to machine accuracy by operating it with $\sum_{lk} g^{lk}$, since

$$\sum_{lk} g^{lk} [\delta_l^i (\Gamma^*)_{kj}^j - g_{lm} g^{ij} (\Gamma^*)_{jk}^m] = 0$$

for arbitrary, symmetric tensor components $(\Gamma^*)_{kl}^i$.

The correction algorithm in Eq. (21) can be extended to the alternative formulation of the equation of motion, Eq. (15) (which is useful for singular coordinate systems). In this case, the Coriolis force-balance condition reads:

$$\partial_n (J g^{ni}) - J g^{ni} \Gamma_{nk}^k + J g^{nk} \Gamma_{nk}^i = 0. \quad (22)$$

Eq. (20) can be rewritten to satisfy Eq. (22) discretely by noting that:

$$g_{lm} \partial_k (g^{mi}) = \frac{g_{lm}}{J} \partial_k (J g^{mi}) - \delta_l^i \Gamma_{kj}^j,$$

to find:

$$\Gamma_{kl}^i = -\frac{g_{lm}}{J} \partial_k (J g^{mi}) + 2\delta_l^i \Gamma_{kj}^j - g_{lm} g^{ij} \Gamma_{jk}^m. \quad (23)$$

This result can also be used in a predictor-corrector fashion, as before.

We emphasize that the numerical cancellation of the Coriolis force-balance condition is facilitated by the fact that the scheme is cell centered, and hence all vector components and geometric magnitudes are known at the same spatial location. That Eq. (21) (or Eq. (23) when applicable) result in the exact cancellation of the Coriolis force-balance condition has been confirmed numerically. Numerical experiments (Section 5.4) have demonstrated that using the corrected value of Γ_{kl}^i instead of $(\Gamma^*)_{kl}^i$ results in significantly improved conservation properties in curvilinear geometry.

4.5. Discretization of Faraday's law

ZIP differencing is not used in Faraday's law. The discretization of Faraday's law (Eq. (11)) should satisfy the solenoidal constraint for the magnetic field $\nabla \cdot \vec{B} = 0$ numerically to round-off. The cell-centered measure of the divergence reads:

$$\nabla \cdot \vec{B}|_{i,j} \approx \frac{B_{i+1,j}^1 - B_{i-1,j}^1}{2h_{1,i}} + \frac{B_{i,j+1}^2 - B_{i,j-1}^2}{2h_{2,j}}, \quad (24)$$

with B^i the contravariant components of \vec{B} . With this measure, Tóth [15] showed that a centered finite differences discretization of Faraday's law (Eq. (7)),

$$\partial_t B^1 + \frac{E_{3,i,j+1} - E_{3,i,j-1}}{2h_{2,j}} = 0; \quad \partial_t B^2 - \frac{E_{3,i+1,j} - E_{3,i-1,j}}{2h_{1,i}} = 0, \quad (25)$$

with E_i the covariant components of \vec{E} , ensures that \vec{B} remains solenoidal to round-off within the domain provided that its initial value is also solenoidal, even in general non-orthogonal representations. The proof is straightforward (insert the time-discrete form of Eq. (25) into (24)). Refer to the numerical results in Section 5 for confirmation.

In Eq. (25), the electric field E_3 is defined at cell centers. The ideal contribution to E_3 , $(\vec{v} \times \vec{B})_3$, can be found trivially from the corresponding cell-centered quantities. The resistive contribution, ηj_3 , requires taking the curl of the magnetic field, which is also discretized using centered differences. While this spreads the discrete stencil of the diffusive term $\nabla \times (\eta \nabla \times \vec{B})$ (i.e. its discretization is not compact), it results in an SPD discrete operator—also in non-orthogonal representations—that exactly preserves \vec{B} and \vec{j} solenoidal to machine accuracy with the divergence measure in Eq. (24).

We note that, since the discretization of Faraday's law is formulated in terms of the electric field components, the proposed discretization (with the solenoidal property) readily applies to extended versions of Ohm's law that include Hall and diamagnetic pressure terms.

It is worth pointing out that the exact conservation of $\nabla \cdot \vec{B} = 0$ avoids the (unphysical) parallel force problem pointed out by Brackbill and Barnes [3] when a conservative formulation of the equation of motion is employed. This is discussed further in Section 4.7.3.

The wary reader might have noticed that Eq. (25) for Faraday's law is equivalent to the FA scheme described in Section 4.1, and might wonder why this is a good choice in this instance. The answer is three-fold. Firstly, this is the *only* choice that results in a divergence-free scheme consistent with the divergence definition in Eq. (24), and we regard this as a superior principle to abide by. Secondly, while Eqs. (25) and (24) support red-black modes for the magnetic field, these are effectively controlled by the use of ZIP in the magnetic field contribution to the equation of motion (checkerboard-like instabilities only grow when supported all relevant equations; for the magnetic field, these are Faraday's law, the solenoidal constraint, and the equation of motion). Finally, regarding the possibility of nonlinear instabilities (antidiffusion), we have not seen any evidence of it in our simulations, even in the case of very coarse meshes and $\eta = 0$ (see Section 5). We conjecture that the solenoidal constraint in Eq. (24) is effectively able to “clamp” down potential antidiffusive nonlinear modes of Eq. (25), as only solenoidal antidiffusive modes can grow. We do not, however, have rigorous proof of this.

We end this section by noting that, even though Eq. (25) ensures that $\nabla \cdot \nabla \times \equiv 0$ within the domain, error can still accumulate at the boundaries unless care is taken. The treatment of the boundary conditions for all quantities in general curvilinear geometry is the subject of the next section.

4.6. Boundary conditions

At boundary cells, domain boundaries align with cell faces. Boundary conditions are imposed by the ghost-cell approach. Ghost cells live outside of the domain, and are placed so that the domain boundary is equidistant between the ghost-cell and the boundary-cell centers. Boundary conditions are imposed by extrapolation across the relevant boundary to the ghost node. Under most circumstances of interest, this provides a second-order approximation of the boundary condition at the boundary face. In what follows, we consider the formulation of usual boundary conditions for MHD in a non-orthogonal representation.

4.6.1. Boundary conditions on density ρ

The boundary condition for the density is derived from the mass conservation constraint. Integrating the continuity equation (1) over the whole plasma volume yields:

$$\partial_t M + \oint \frac{dS}{\|\vec{n}\|} \vec{n} \cdot (\rho \vec{v} - D \nabla \rho) = 0,$$

where M is the total mass and \vec{n} is a vector normal to the boundary surface ξ_n ($\vec{n} = \nabla \xi_n$). Conservation of mass enforces $\partial_t M = 0$, which for arbitrary geometries requires $\vec{n} \cdot (\rho \vec{v} - D \nabla \rho) = 0$ locally at the boundary. The impenetrable wall boundary condition (see the next section) enforces $\vec{n} \cdot \vec{v} = 0$, and hence the conservative density boundary condition (homogeneous Neumann) reads:

$$\vec{n} \cdot \nabla \rho = 0.$$

In non-orthogonal representations, since $\vec{n} = \nabla \xi_n$, we find $\vec{n} \cdot \nabla = g^{nm} \partial_m$. Consequently, the homogeneous Neumann boundary condition on ρ at the ξ_n boundary reads:

$$\vec{n} \cdot \nabla \rho = 0 \Rightarrow \partial_n \rho = - \sum_{m \neq n} \frac{g^{nm}}{g^{nn}} \partial_m \rho, \quad (26)$$

where no sum on n is intended. In 2D, and specializing for $n = 1$, this condition would be discretized as:

$$\rho_{i+1,j} = \rho_{i,j} - h_{1,i+1/2} \frac{g^{12}}{g^{11}} \Big|_{i,j} \frac{\rho_{i,j+1} - \rho_{i,j-1}}{2h_{2,j}}. \quad (27)$$

This discretization approximates Eq. (26) only to first order in h_1 due to the centering of the geometric correction term at (i, j) . However, it provides a simple prescription to fill ghost nodes that does not require one to solve a coupled problem for the ghost-cell values. This choice is not expected to affect the overall second-order accuracy of the difference scheme because the correction term in Eq. (27) is affected by the ratio g^{12}/g^{11} , which is zero for orthogonal meshes (and then Eq. (27) is second-order accurate), and small for mildly non-orthogonal meshes. Refer to Section 5.4 for numerical confirmation.

4.6.2. Boundary conditions on plasma velocity \vec{v}

At boundaries, the vector components of interest are the normal component $\vec{v}_n = (\vec{n} \cdot \vec{v}) \vec{n} / \|\vec{n}\|^2$ and the tangential component $\vec{v}_t = \vec{n} \times (\vec{v} \times \vec{n}) / \|\vec{n}\|^2$. For the flow field, the usual boundary condition for the normal component is impenetrable wall ($\vec{n} \cdot \vec{v} = 0$), while for the tangential component it could be either no-slip ($\vec{v}_t = \vec{0}$) or no-stress. Next, we study each option in detail. It should be borne in mind that the logical formulation of the MHD equations (Section 3) employs the *contravariant* components of the velocity, and hence this is the representation of choice for velocity boundary conditions.

4.6.2.1. Normal component: impenetrable wall $\vec{n} \cdot \vec{v} = 0$. By the definitions in Section 3, this condition trivially translates into $v^n = 0$.

4.6.2.2. Tangential component: no slip $\vec{v}_t = \vec{0}$. A necessary and sufficient condition for $\vec{v}_t = \vec{0}$ is $\vec{v} \times \vec{n} = \vec{0}$, which in turn implies that $v_k = 0$, with $k \neq n$ (i.e. the covariant components of the velocity corresponding to the tangential directions are identically zero). In terms of the contravariant components of the velocity, we employ the coordinate transformation relation $v^i = g^{ik} v_k$ and the fact that the two tangential covariant components of the velocity vanish, to obtain:

$$v^k = v^n g^{nk} / g^{nn}, \quad k \neq n \quad (28)$$

(no sum intended). When Eq. (28) is combined with the impenetrable wall boundary condition ($v^n = 0$), there results $v^i = 0, \forall i$ (i.e. $\vec{v} \equiv \vec{0}$).

4.6.2.3. Tangential component: no stress. The no-stress condition specifies that the boundary exert no viscous stress on the plasma flow, thus allowing a free-streaming tangential flow. A rigorous derivation of this boundary condition (also called “tangency” condition [23], because it pertains to the flow tangent to the boundary surface), based on the conservation of angular momentum, is presented in Appendix B, and concludes that the velocity at the boundary should satisfy:

$$\vec{n} \cdot (\nabla \vec{v}) \times \vec{n} = \vec{0}. \quad (29)$$

Crossing this result with \vec{n} and projecting onto the tangential vectors, yields $\vec{n} \cdot [\nabla \vec{v}] \cdot \underline{l} = 0, l \neq n$. This we readily recognize as a generalized homogeneous Neumann boundary condition for the tangential velocity components. Expressing this result in logical coordinates gives (Appendix A) $g^{nm}(\partial_m v_l - \Gamma_{lm}^k v_k) = 0, l \neq n$, which, upon isolating the normal derivative term, results in the following tangency condition:

$$\partial_n v_l = - \sum_{m \neq n} \frac{g^{nm}}{g^{nn}} \partial_m v_l + \sum_{m,k} \frac{g^{nm}}{g^{nn}} \Gamma_{lm}^k v_k, \quad l \neq n, \quad (30)$$

where all quantities in the right-hand side are known, and no sum in n is intended. This is the generalization of the scalar Neumann boundary condition in Eq. (26) for the tangential velocity components, and is discretized in a similar fashion.

Eq. (30) determines the *covariant* velocity components at the ghost cells. In order to fill the ghost nodes of the *contravariant* velocity components using the previous result, the following procedure is employed:

- (1) At *inner* boundary cells, *covariant* velocity components are found from the contravariant components via $v_i = g_{ik} v^k$.
- (2) At ghost cells, the tangential *covariant* velocity components are found from Eq. (30).
- (3) At ghost cells, the normal *covariant* velocity component v_n is found from the contravariant normal component v^n —known from the impenetrable wall condition—and the tangential covariant components—known from step 2—using $v^n = g^{nj} v_j$ (where only v_n in the right-hand side is unknown), as follows:

$$v_n = \frac{1}{g^{nn}} \left[v^n - \sum_{j \neq n} g^{nj} v_j \right].$$

- (4) At this point, all covariant velocity components are known at the ghost cells. The tangential *contravariant* velocity components are found from $v^j = g^{jk} v_k$.

4.6.3. Boundary conditions on the magnetic field \vec{B}

As with the velocity field, boundary conditions are applied to normal and tangential components of the magnetic field. However, these are not entirely independent, since they are related by the local solenoidal constraint, $\nabla \cdot \vec{B} = 0$. While this condition is automatically satisfied within the domain by the discretization proposed in Eq. (25), it is at the heart of the boundary treatment of the magnetic field. The next sections describe these issues further.

4.6.3.1. Solenoidal condition for the normal component. The discrete solenoidal requirement (Eq. (24)) imposes a constraint on the normal component of the magnetic field at a given boundary, independent of other electromagnetic physics. For instance, considering the $i = 1$ boundary, the normal component of the magnetic field B^1 at the ghost node $i = 0$ can be readily found from Eq. (24) as:

$$B_{i=0,j}^1 = B_{i=2,j}^1 - h_{1,i=1} (B_{i=1,j+1}^2 - B_{i=1,j-1}^2) / h_{2,j},$$

where all magnitudes in the right-hand side are within the domain, and hence known. This ensures that there is no divergence error at the boundary, and, together with the discretization of Faraday's law outlined above, enforces a solenoidal magnetic field everywhere at all times. This strategy is similar to that employed in [24] to enforce Gauss' law $\nabla \cdot \vec{E} = en/\epsilon_0$ in the electromagnetic PIC method context.

4.6.3.2. Boundary conditions for the tangential components. The boundary conditions for the tangential magnetic field components depend strongly on the electromagnetic physics at the boundary of interest. Here, we consider a *perfectly conducting wall*, which supports no tangential electric field ($\vec{n} \times \vec{E} = \vec{0}$) and allows no magnetic flux ($\vec{n} \cdot \vec{B} = 0$). For finite resistivity, these constraints imply that the tangential current must vanish ($\vec{n} \times \vec{j} = \vec{0}$) at the boundary, since, from Eq. (7):

$$\vec{n} \times \vec{E} = -\vec{n} \times (\vec{v} \times \vec{B}) + \eta \vec{n} \times \vec{j} = \vec{0},$$

and $\vec{n} \times (\vec{v} \times \vec{B}) = \vec{0}$ for impenetrable ($\vec{n} \cdot \vec{v} = 0$), perfectly conducting walls ($\vec{n} \cdot \vec{B} = 0$). In terms of its contravariant components, the $\vec{n} \times \vec{j} = \vec{0}$ condition translates into (Eq. (28)):

$$j^k = j^n \frac{g^{nk}}{g^{nn}}, \quad k \neq n, \quad (31)$$

(no sum intended) which relates the contravariant tangential (j^k) and normal (j^n) components of the current. We relate this condition to the magnetic field components by recalling that, in the logical representation, $j^m = \epsilon_{mnl} \partial_n B_l$, to find:

$$\partial_n B_j = \partial_j B_n + \frac{g^{nk}}{g^{nn}} [\partial_j B_k - \partial_k B_j], \quad k \neq j \neq n. \quad (32)$$

Again, all right-hand side quantities are known, and this equation is discretized similarly to other examples given above. We note that, as with the no-stress velocity condition, Eq. (32) deals with the covariant components of the magnetic field, while the logical formulation of the MHD equations (Section 3) is in terms of its contravariant components. The same procedure outlined for the velocity in Section 4.6.2 is employed here for the magnetic field, except that the normal contravariant magnetic field component B^n is found from the solenoidal condition, and Eq. (32) is used to find the tangential covariant magnetic field components at the ghost cells.

4.6.4. Boundary conditions on the electrical current \vec{j}

The previous discussion has focused on the boundary conditions of the magnetic field components. However, the current components are also needed at the ghost cells to calculate the resistive term in Faraday's law at boundary cells. We could find them from the magnetic field by using $\vec{j} = \nabla \times \vec{B}$. However, the curl operation at the ghost cells requires a special treatment to achieve second order accuracy (one-sided difference schemes), and it propagates

inaccuracies in the calculation of the magnetic field components at the boundary. A much better approach, which does not involve derivatives of the magnetic field, is to use the solenoidal constraint of the current ($\nabla \cdot \vec{j} = 0$) to find the normal contravariant components at the boundaries (thus ensuring that $\nabla \cdot \vec{j} = 0$ everywhere in the domain), and then use Eq. (31) to find the corresponding tangential contravariant components from the normal component. This is the procedure employed here.

4.6.5. Boundary conditions on pressure p (or temperature T)

The pressure boundary condition enforces the momentum balance locally at the plasma boundary. We derive it from the non-conservative form of the equation of motion, which reads:

$$\rho[\partial_t \vec{v} + \vec{v} \cdot \nabla \vec{v} - \nabla \cdot (\nu \nabla \vec{v})] = \vec{j} \times \vec{B} - \nabla p.$$

Projecting this equation along the normal direction at the boundary, and taking into account that $\vec{n} \cdot \vec{v} = 0$ (impenetrable wall) and $\vec{n} \times \vec{j} = 0$ (perfectly conducting wall), we find the momentum balance condition:

$$\rho \vec{v} \cdot (\nabla \vec{v}) \cdot \vec{n} - \rho \nabla \cdot (\nu \nabla \vec{v}) \cdot \vec{n} = -\vec{n} \cdot \nabla p.$$

In plasmas, the perpendicular viscosity coefficient depends inversely on the plasma temperature ($\nu_\perp \sim T^{-1/2}$) [25,26]. We consider two scenarios. In the cold boundary-plasma limit, the plasma viscosity term is dominant and the pressure and inertial terms become irrelevant. In this limit, a homogeneous Dirichlet boundary condition for pressure (or temperature) is usually employed [8]. In the warm boundary-plasma limit, however, the plasma viscosity is negligible, and the pressure boundary condition becomes:

$$\vec{n} \cdot \nabla p = \rho \vec{v} \cdot (\nabla \vec{v}) \cdot \vec{n}.$$

The right-hand side term can be rewritten as $\vec{v} \cdot (\nabla \vec{v}) \cdot \vec{n} = \vec{v} \cdot \nabla (\vec{v} \cdot \vec{n}) - \vec{v} \cdot (\nabla \vec{n}) \cdot \vec{v}$. Recalling that $\vec{v} \cdot \vec{n}$ is constant (vanishes) at the plasma boundary, it follows that $\vec{v} \cdot \vec{n}$ is a surface quantity, and hence $\nabla (\vec{v} \cdot \vec{n}) \parallel \vec{n}$. Therefore, $\vec{v} \cdot \nabla (\vec{v} \cdot \vec{n}) \propto \vec{v} \cdot \vec{n} = 0$, and the pressure boundary condition reads:

$$\vec{n} \cdot \nabla p = \rho \vec{v} \cdot (\nabla \vec{n}) \cdot \vec{v}. \quad (33)$$

The physical interpretation of this result becomes obvious in cylindrical coordinates, where it gives $\partial_r p = \rho v_\theta^2 / r$, i.e. the pressure force balances the inertial (centrifugal) force locally at the boundary.

In terms of temperature, Eq. (33) becomes (using $p = 2\rho T$ and $\vec{n} \cdot \nabla p = 0$):

$$\vec{n} \cdot \nabla T = \frac{1}{2} \vec{v} \cdot (\nabla \vec{n}) \cdot \vec{v},$$

which, in the logical coordinates representation, reads:

$$\partial_n T = - \sum_{m \neq n} \frac{g^{nm}}{g^{nn}} \partial_m T - \sum_{m,k} \frac{\Gamma_{mk}^n}{2Jg^{nn}} v^m v^k.$$

This result is discretized similarly to Eq. (26).

4.6.6. Boundary conditions at singular points

At singular points, the cell volume vanishes and one or more of the coordinates (usually angular) become degenerate. This is the case, for example, at $r = 0$ in cylindrical, toroidal, and spherical coordinates.

Our discretization of choice places control volumes around the singular point, so that boundary faces coincide with the singular point. For equations in divergence form, this arrangement is particularly suitable, since fluxes across singular-point boundaries are identically zero owing to geometric reasons (i.e. the area of the cell boundary vanishes at the singular point). However, there are equations that are not in divergence form, and a proper discretization requires knowledge of relevant quantities at the singular point. Notably, this is the case of Faraday's

law, which requires knowledge of the electric field at the singular point (which, in turn, requires knowledge of the magnetic field, current, momentum, and density).

The next sections describe how singular points are treated here. Before we proceed, however, we note that the treatment of scalars and vectors at the singular point is markedly different. Scalars are, by definition, well-defined quantities regardless of the coordinate representation. Vectors as entities are also well defined, but their component representation is not: vector components expressed in the singular coordinate representation at the singular point are multivalued. This and other issues are discussed further below.

4.6.6.1. Singular-point boundary condition for scalars. As mentioned previously, scalars are well defined (single-valued) at the singular point. Here, we find the scalar value of interest (ρ , T) by interpolation from the control volumes surrounding it. The procedure is as follows. For each angular value, we extrapolate the scalar radially to the singular point $r = 0$ using second-order formulas. The extrapolated values are then volume-averaged in the angular direction, thus providing a unique interpolated value of the scalar at the singular point.

4.6.6.2. Singular-point boundary condition for vectors. Vector components in the singular representation are multi-valued. This can readily be seen with a specific example in cylindrical coordinates. Consider the velocity vector in cylindrical coordinates $\vec{v} = v_r \hat{r} + v_\theta \hat{\theta} + v_z \hat{z}$, where \hat{r} , $\hat{\theta}$, and \hat{z} are the cylindrical unit vectors. Consider the same vector at the same location, but expressed in Cartesian coordinates $\vec{v} = v_x \hat{x} + v_y \hat{y} + v_z \hat{z}$. Trivially, we know that $v_r = v_x \cos(\theta) + v_y \sin(\theta)$, $v_\theta = -v_x \sin(\theta) + v_y \cos(\theta)$. While the Cartesian components are always well-defined, the cylindrical components at the singular point $r = 0$ change with θ (which is degenerate).

This realization dictates the strategy to deal with vectors at singular points. We use the same interpolation strategy as with scalars, but on the Cartesian components of the vector. This requires a local transformation from curvilinear (covariant, contravariant) to Cartesian components at the cell centers around the singular point, and provides a unique Cartesian representation of the vector in question at the singular point. This vector is then transformed back to curvilinear components using a very small (but finite) value for the radius $r \sim \sqrt{\epsilon}$ (where ϵ represents the machine accuracy). A finite radius is necessary to avoid numerical indetermination of terms of the form r/r that occur in the calculation of the metric tensor elements.

4.7. Further considerations about the spatial scheme

4.7.1. Monotonicity

The proposed spatial scheme is second-order and non-dissipative, as evidenced by the spatial truncation errors of ZIP (Section 4.1) and the results in Section 5. While the absence of numerical dissipation (and anti-dissipation) conserves energy and ensures nonlinear stability, it may cause monotonicity problems in situations where large flows are present (i.e. in advection-dominated instances) since ZIP is not total-variation-diminishing (TVD). For these instances, a more sophisticated advection scheme is needed in order to avoid spurious oscillations. We envision combining ZIP with a monotonic scheme such as SMART [19]. SMART is a flexible monotonic discretization scheme that recycles non-monotonic schemes when there is no risk of non-monotonic behavior, and reverts to a TVD scheme otherwise. This extension is left for future work.

4.7.2. Special considerations around singular points

In addition to the singular-point boundary conditions described above, there are a few idiosyncrasies of the discretization around singular-points that deserve further comment. We focus our discussion using cylindrical coordinates as a paradigm of a singular representation, but the ideas here extend easily to other singular-point representations.

For cylindrical coordinates, and using the conventions put forth in Section 3, the contravariant components of a vector A read, in terms of the usual cylindrical components, $A^1 = J A_r$, $A^2 = A_\theta$, and $A^3 = J A_z$, with $J = r$ the Jacobian. Because $J \rightarrow 0$ in the neighborhood of the singular point, the ZIP interpolation, as stated in Section 4.1,

may introduce $\mathcal{O}(1)$ errors. The way this is resolved is best understood with our example advection equation $\partial_t \Phi + \nabla \cdot (\vec{v} \Phi) = 0$, which in the logical representation reads (considering only the radial contribution):

$$\partial_t J \Phi + \partial_1 (\Phi v^1) = 0.$$

Since v^1 scales with J , we consider the equivalent formulation to avoid large interpolation errors near the singular point:

$$\partial_t J \Phi + \partial_1 \left(J \Phi \frac{v^1}{J} \right) = 0.$$

When applying ZIP, we group v^1/J , and the ZIP flux reads:

$$f_{i+1/2} = J_{i+1/2} \frac{\Phi_{i+1}(v^1/J)_i + \Phi_i(v^1/J)_{i+1}}{2}.$$

This removes the r scaling from v^1 , while still being conservative, and produces accurate interpolations. In order to ensure conservation, this modified discretization is used everywhere in the domain.

4.7.3. Momentum conservation and parallel body force

Brackbill and Barnes [3] pointed out that spatial difference schemes that conserve momentum but do not preserve $\nabla \cdot \vec{B} = 0$ to round-off would produce an unphysical body force parallel to the magnetic field. In conservative form, the Lorentz force reads $\vec{F} = \vec{j} \times \vec{B} = \nabla \cdot [\vec{B} \vec{B} - \vec{T} B^2/2]$. Clearly, while the non-conservative form satisfies the orthogonality property $\vec{F} \cdot \vec{B} = (\vec{j} \times \vec{B}) \cdot \vec{B} = 0$ both in the continuum and in the discrete, the conservative form does not satisfy this property in the discrete whenever $\nabla \cdot \vec{B} \neq 0$, since [3]:

$$\vec{F} \cdot \vec{B} = B^2 \nabla \cdot \vec{B}. \quad (34)$$

In Ref. [15], Tóth claims that, even in Cartesian coordinates, a “perfect scheme” that satisfies both the orthogonality property and momentum conservation does not exist, even if the scheme satisfies $\nabla \cdot \vec{B} = 0$ discretely for some difference approximation of the divergence operator.

We proceed to show that, in the specific case of Cartesian coordinates, our proposed scheme does satisfy both exact momentum conservation and the orthogonality property in the discrete sense. At the heart of the proof is the chain rule property satisfied by ZIP. In Cartesian coordinates, the components of the Lorentz force read:

$$\begin{aligned} F_x &= \partial_x (B_x^2) + \partial_y (B_x B_y) - \partial_x (B^2/2), \\ F_y &= \partial_x (B_x B_y) + \partial_y (B_y^2) - \partial_y (B^2/2). \end{aligned}$$

Using ZIP differencing to discretize these terms at the cell (i, j) , and owing to the chain rule property of ZIP, we find straightforwardly that:

$$\begin{aligned} F_{xi,j} &= B_{xi,j} \left[\frac{B_{xi+1,j} - B_{xi-1,j}}{2h_{x,i}} + \frac{B_{yi,j+1} - B_{yi,j-1}}{2h_{y,j}} \right] \\ &\quad + B_{yi,j} \left[\frac{B_{xi,j+1} - B_{xi,j-1}}{2h_{y,j}} - \frac{B_{yi+1,j} - B_{yi-1,j}}{2h_{x,i}} \right], \\ F_{yi,j} &= B_{xi,j} \left[\frac{B_{yi+1,j} - B_{yi-1,j}}{2h_{x,i}} - \frac{B_{xi,j+1} - B_{xi,j-1}}{2h_{y,j}} \right] \\ &\quad + B_{yi,j} \left[\frac{B_{xi+1,j} - B_{xi-1,j}}{2h_{x,i}} + \frac{B_{yi,j+1} - B_{yi,j-1}}{2h_{y,j}} \right]. \end{aligned}$$

Therefore,

$$\begin{aligned}\vec{F} \cdot \vec{B}|_{i,j} &= F_{xi,j} B_{xi,j} + F_{yi,j} B_{yi,j} \\ &= (B_{xi,j}^2 + B_{yi,j}^2) \left[\frac{B_{xi+1,j} - B_{xi-1,j}}{2h_{x,i}} + \frac{B_{yi,j+1} - B_{yi,j-1}}{2h_{y,j}} \right] = B_{i,j}^2 \nabla \cdot \vec{B}|_{i,j},\end{aligned}\quad (35)$$

which vanishes exactly owing to Eq. (24). We note that Eq. (35) is exactly the discrete form of the continuum result, Eq. (34).

We conclude that, in Cartesian coordinates, both the momentum conservation and the orthogonality property are exactly satisfied in the discrete sense. This occurs because the discrete measure of the divergence operator in Eq. (24) exactly coincides with the measure required for the cancellation of $\vec{F} \cdot \vec{B}|_{i,j}$. Unfortunately, this result does not carry over to general curvilinear coordinates, since exact momentum conservation is not generally possible due to Coriolis forces (see Section 3), and geometric factors prevent the exact cancellations that lead to Eq. (35) in Cartesian coordinates. In general curvilinear coordinates, both properties are only satisfied to truncation error.

4.7.4. Preservation of the conservation properties by the implicit solver

While the spatial scheme has been constructed to preserve the conservation properties of the continuum MHD model, one could argue that the details of the temporal discretization and the implicit solver (such as finite linear and nonlinear convergence tolerances) could spoil the exact numerical cancellation provided by the scheme. We prove in Appendix C that, under very general assumptions, the conservation properties are preserved by the Newton–Krylov implicit algorithm regardless of these details. Numerical confirmation of this is presented in the next section.

5. Numerical tests

We perform five 2D numerical tests that demonstrate the properties of the scheme: (1) propagation of a magnetosonic wave on a Cartesian grid, (2) the ideal MHD Kelvin–Helmholtz instability (KH) on a Cartesian grid, (3) the resistive tearing instability (TM) on a Cartesian grid, (4) the resistive tearing instability on a non-orthogonal (sinusoidal) grid, and (5) the $m = 1$ ideal kink instability in a screw pinch in helical coordinates. Test 1 demonstrates the lack of numerical dissipation of the spatial scheme in the absence of physical dissipation. Test 2 demonstrates the linear and nonlinear stability of the spatial scheme in the absence of physical dissipation. Tests 3 and 4 demonstrate the preservation of the solenoidal constraint with nontrivial magnetic fields, in both orthogonal and nonorthogonal grid representations. And test 5 shows the performance of the scheme in the presence of singular points.

Most tests are performed in very coarse meshes (32×32 unless otherwise specified) on purpose, to test the accuracy of the scheme in unfavorable conditions. Some selected results are performed with finer grids to demonstrate convergence properties. The results have been benchmarked by comparing growth rates and eigenmode structures obtained with a linear eigenvalue solver for the configurations of interest.

Computations have been performed implicitly using the Jacobian-free Newton–Krylov implicit algorithm described in Refs. [27,28], but without any preconditioning. While the lack of preconditioning results in a non-optimal implicit solver, it is suitable for the purpose of testing and benchmarking the spatial scheme. Future work will concentrate on the development of a suitable physics-based preconditioning strategy, in the same fashion as in Refs. [27,28]. All results presented here employ a linear GMRES tolerance of 0.05 per Jacobian solve, a relative residual tolerance of 10^{-4} per nonlinear solve, and feature a second-order Crank–Nicolson temporal scheme.

5.1. Magnetosonic wave propagation

The purpose of this test is to demonstrate the lack of numerical dissipation of the scheme in the absence of physical diffusion. This in turn is indirect evidence that the spatial scheme is second-order accurate in space as

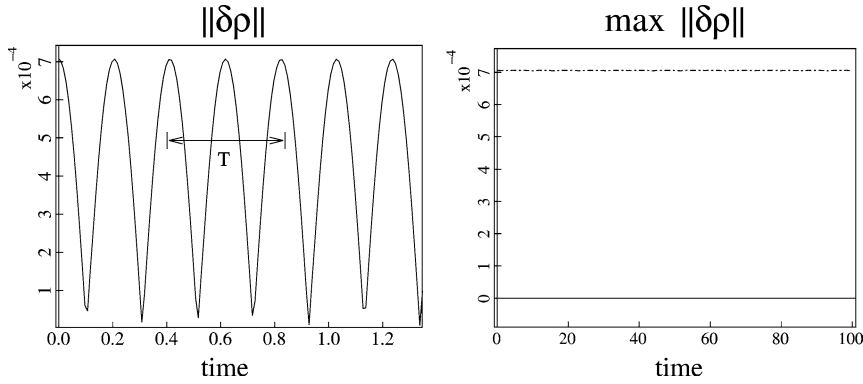


Fig. 2. Euclidean (ℓ_2) norm of the density perturbation in the magnetosonic wave test. Shown are a detail of the time history (left) and the time history of the local maxima (right). The latter shows that there is no amplitude decay in time, and the former shows the period T , which is equal to the theoretical prediction of 0.408.

well as time, since first-order spatial and/or temporal errors of advective terms are diffusive in nature. Direct evidence of the second-order nature of the scheme for a curvilinear grid is presented in Section 5.4. The equilibrium is defined by uniform density and temperature ($\rho_0 = T_0 = 1$), uniform magnetic field in the ignorable direction ($B_{x0} = B_{y0} = 0$, $B_{z0} = 1$), and zero plasma velocity. The computation is performed in a 2D rectangular domain 1×1 , with $\eta = \nu = D = 0$, $\gamma = 1$. The boundary conditions are periodic in both x and y . In this configuration, the MHD system supports a magnetosonic wave of frequency $\omega = \pm\sqrt{3}k$, with $k^2 = k_x^2 + k_y^2$, and $k_x = k_y = 2\pi$. We initialize the mode with perturbations $\delta\rho = \delta B_z = \epsilon \cos(\vec{k} \cdot \vec{x})$, with $\epsilon = 10^{-3}$, which set off a standing magnetosonic wave of period $T = 2\pi/\omega \approx 0.408$. The Euclidean (ℓ_2) norm of the perturbation of the density, $\|\delta\rho\|_2(t) = \sum_{i,j} dV_{i,j}(\rho - \rho_0)_{i,j}^2$, is given in Fig. 2, showing the oscillatory behavior. The numerical frequency agrees with the analytical result. Note that the amplitude does not decay in time despite the large number of cycles run (~ 250 cycles), thus demonstrating the lack of numerical dissipation.

5.2. Ideal Kelvin–Helmholtz instability in Cartesian coordinates

The purpose of this test is to demonstrate the stability of spatial scheme in the absence of physical dissipation. The equilibrium is defined by uniform density and pressure ($\rho_0 = T_0 = 1$), uniform magnetic field in the ignorable direction ($B_{x0} = B_{y0} = 0$, $B_{z0} = 1$), and a sheared velocity profile

$$v_{y0} = V_0 \tanh[(x - 0.5)/\lambda],$$

with $V_0 = 0.5$ and $\lambda = 0.2$. The computation is performed in a 2D rectangular domain 1×2.5 , and with $\eta = \nu = D = 0$, $\gamma = 5/3$. The boundary conditions are periodic in y and perfect conductor ($B_x = 0$), no stress ($\partial_x v_y = 0$), and impenetrable wall ($v_x = 0$) boundary conditions in x . Homogeneous Neumann boundary conditions are imposed for both ρ and T .

The linear eigenvalue solver predicts a growth rate $\gamma_{EV} = 0.287$. The initial value calculation finds $\gamma_{EV} = 0.283$ in a 32×32 grid, and $\gamma_{EV} = 0.290$ in a 64×64 grid. Fig. 3 depicts time histories and contours plots at early saturation of selected quantities. Quantities chosen for the time histories are:

- Euclidean norm of the perturbation in the x -component of the momentum, $\|\delta p_x\|_2(t) = \sum_{i,j} dV_{i,j}(p_x - p_{x,0})_{i,j}^2$.
- Change in total mass, $\Delta M(t) = \sum_{i,j} dV_{i,j}(\rho - \rho_0)_{i,j}$.
- Change in total momentum components, $\Delta P_k(t) = \sum_{i,j} dV_{i,j}(p_k - p_{k,0})_{i,j}$, with $k = x, y$.

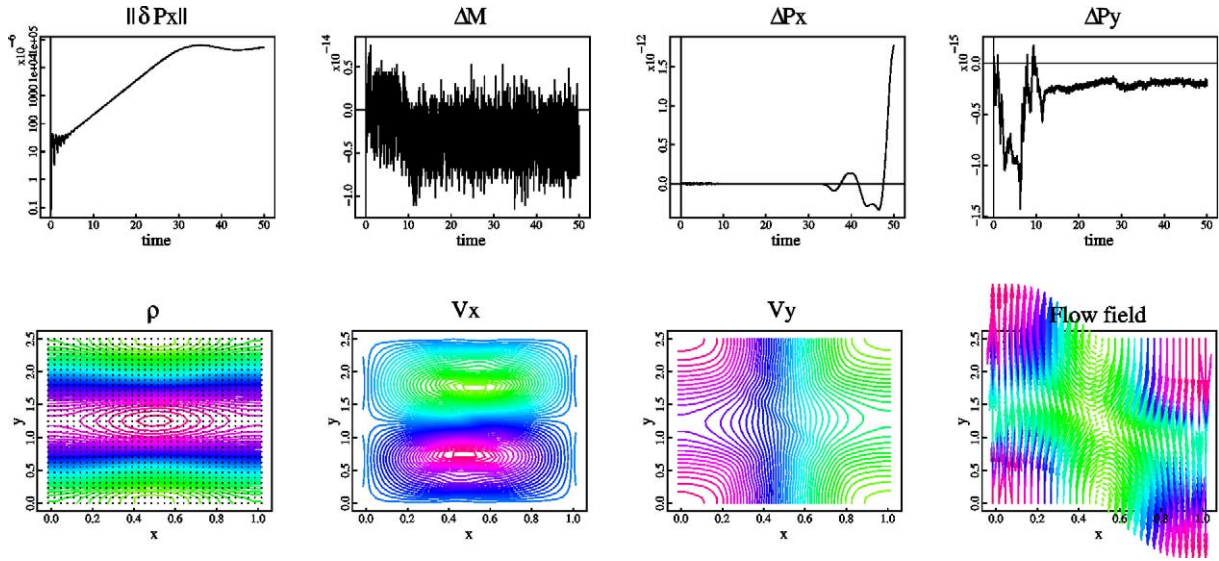


Fig. 3. Results from the simulation of the KH instability in Cartesian. Top figures show time histories of: the Euclidean norm of δp_x , the instantaneous change in the total mass ΔM , and the instantaneous change in the total components of the momentum ΔP_x , ΔP_y . Bottom figures show contour plots of the density (with the grid overlaid), v_x , v_y , and the velocity vector field at early saturation.

Here, the subscript “0” indicates $t = 0$. Clearly, mass and momentum are conserved to roundoff, despite a finite nonlinear tolerance. The solution remains clean despite the absence of dissipation, demonstrating the stability of the scheme. (The solution does develop non-smooth features later in the simulation due to a nonlinear energy cascade to larger wavenumbers, which requires some physical dissipation to be smoothed at the grid scale.)

5.3. Resistive tearing instability in Cartesian coordinates

This test demonstrates preservation of $\nabla \cdot \vec{B} = 0$ with highly structured magnetic fields. The equilibrium is defined by a uniform density and temperature, no flow, and a force-free magnetic Harris-sheet configuration given by:

$$B_{x0} = 0, \quad B_{y0}(x) = \tanh[(x - 0.5)/\lambda], \quad B_{z0} = \sqrt{1 - B_{y0}^2(x)},$$

with $\lambda = 0.2$. The domain is again rectangular of dimensions 1×4 , and we employ Cartesian coordinates. The computation is performed with $\eta = 10^{-2}$, $\nu = 10^{-3}$, $D = 0$, and $\gamma = 5/3$. Boundary conditions are identical to the previous problem. Note that the magnitude of the dissipation coefficients is small for the resolution considered (32×32).

For the tearing instability, the linear eigenvalue solver predicts a growth rate $\gamma_{EV} = 0.098$. The initial value calculation finds $\gamma_{EV} = 0.092$ in a 32×32 grid, and $\gamma_{EV} = 0.097$ in a 64×64 grid. Fig. 4 depicts time histories and contours plots at saturation of selected quantities. In addition to the quantities defined previously, here we plot the ℓ_1 -norm of the divergence of \vec{B} , $\|\nabla \cdot \vec{B}\|_1(t) = \sum_{i,j} dV_{i,j} |\nabla \cdot \vec{B}|_{i,j}$.

Again, mass, momentum, and the solenoidal constraint are conserved to roundoff during the span of the simulation. Note that ρ at saturation appears smooth despite having $D = 0$. The poloidal magnetic flux Ψ (found from the poloidal magnetic field $\vec{B}_p = \nabla \Psi \times \vec{z}$ by a quadrature) clearly shows the magnetic island at saturation.

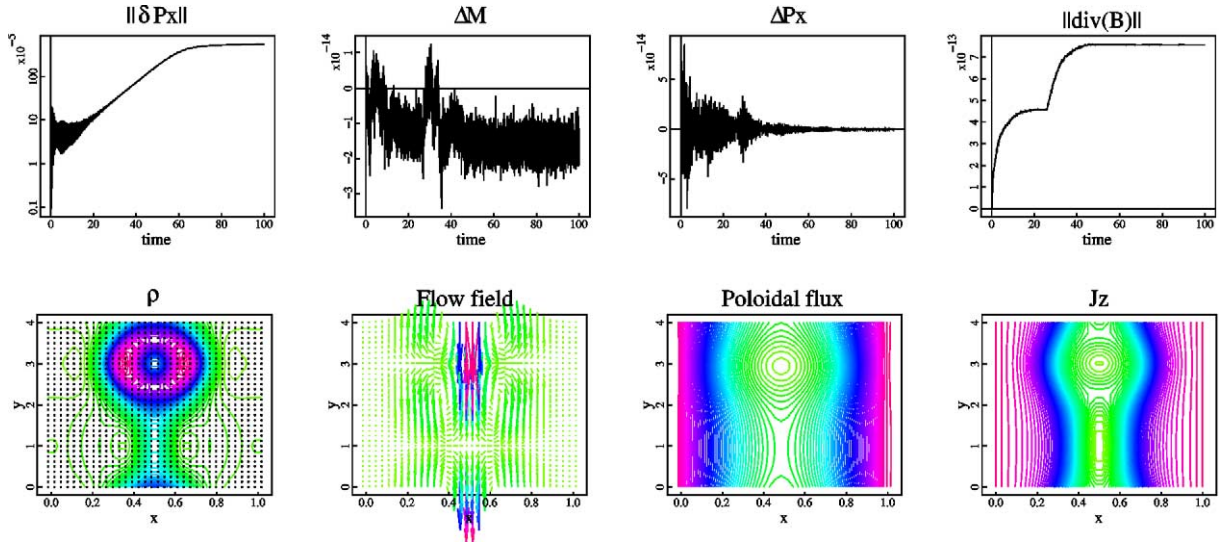


Fig. 4. Results from the simulation of the tearing instability in Cartesian coordinates. Top figures show time histories of: the Euclidean norm of δp_x , the instantaneous change in the total mass ΔM , and the instantaneous change in the total X-component of the momentum ΔP_x , and the ℓ_1 -norm of $\nabla \cdot \vec{B}$. Bottom figures show contour plots of the density (with the grid overlaid), flow field, poloidal magnetic flux, and perpendicular current J_z at saturation.

5.4. Resistive tearing instability in sinusoidal grid

The ability of the algorithm to deal with general, non-orthogonal representations is demonstrated next. We employ the same equilibrium as in the previous tearing instability test. However, the Cartesian grid is perturbed sinusoidally as follows:

$$x = \xi_1 + \epsilon \sin\left(\frac{2\pi}{L_x}\xi_1\right) \sin\left(\frac{2\pi}{L_y}\xi_2\right), \quad y = \xi_2 + \epsilon \sin\left(\frac{2\pi}{L_x}\xi_1\right) \sin\left(\frac{2\pi}{L_y}\xi_2\right).$$

The magnitude of the perturbation is $\epsilon = -0.05$. The grid is setup so that it is aligned with the magnetic field rational surface at $x = 0.5$ (see Fig. 5).

The solution to this problem should reproduce the result obtained in the previous section. The eigenvalue obtained from the initial value calculation is $\gamma_{EV} = 0.091$ in a 32×32 grid and $\gamma_{EV} = 0.097$ in a 64×64 grid, again very close to the predicted growth rate of $\gamma_{EV} = 0.098$. Fig. 5 depicts the same quantities as in the Cartesian tearing mode. Errors in mass and momentum conservation are comparable to the Cartesian case, owing to the numerical cancellation of the Coriolis force-balance condition (Section 4.4.3). The solenoidal constraint is also preserved to round-off. The contour plots demonstrate that the solution is indeed very similar to the Cartesian one, despite the coarseness of the grid. A slight asymmetry in the solution, not observed in the Cartesian case, is introduced by the 32×32 grid, which is too coarse; the asymmetry all but disappears with a 64×64 grid (not shown).

We use this non-orthogonal, curvilinear configuration to demonstrate that the scheme is second-order accurate. For this purpose, we perform a reference simulation with a very fine mesh with 256×256 nodes, using an implicit time step $\Delta t = 10^{-3}$, for 100 time steps. Such a small time step is chosen to ensure that the temporal truncation error is sufficiently small that it does not mask the spatial error results. Computations performed on coarser grids employ the same implicit time step, and are compared against this reference result. We choose the first component

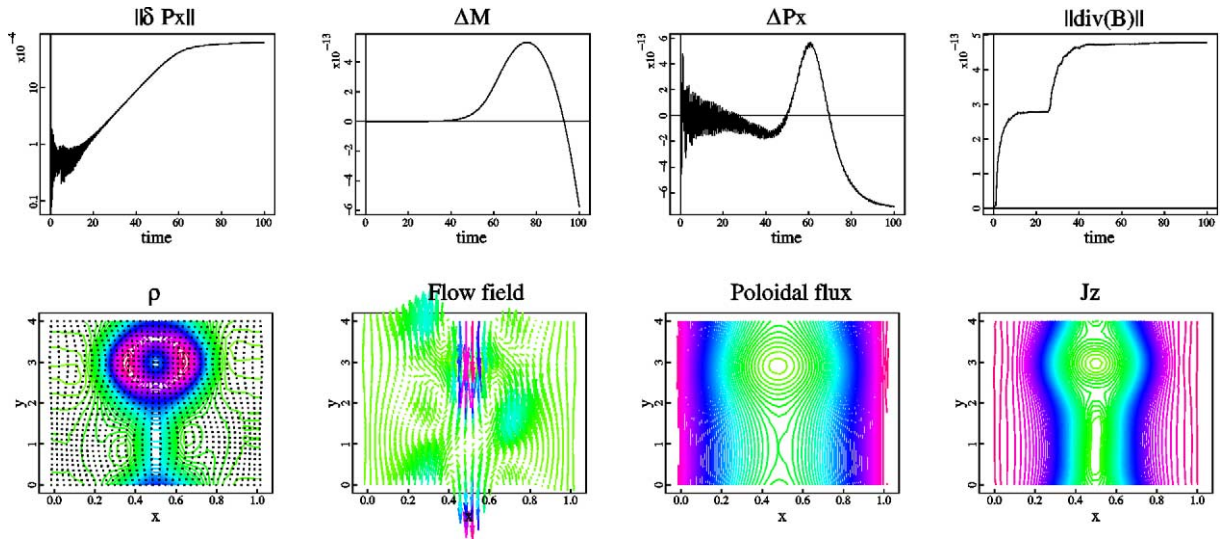


Fig. 5. Results from the simulation of the tearing instability in sinusoidal coordinates. Figs. depict the same quantities as in the Cartesian tearing mode case.

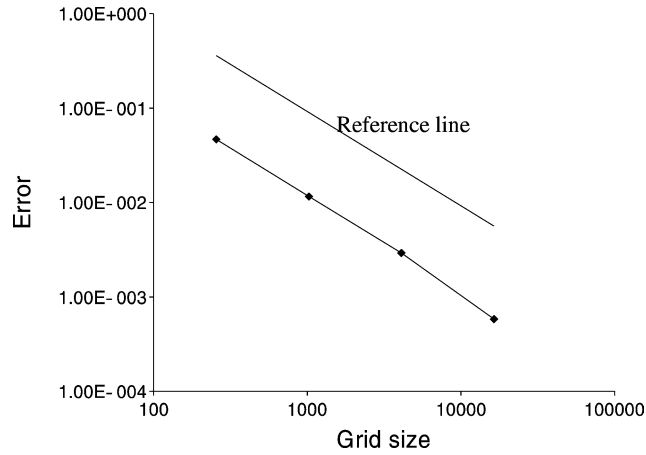


Fig. 6. Results of the grid convergence study performed using the tearing mode problem with the sinusoidal grid. The reference line depicts exact second-order scaling.

of the momentum, P^1 for the comparison. A relative error is computed as follows:

$$E_{\text{rel}} = \sqrt{\frac{\sum_{i,j \in \text{grid}} J_{i,j} (P_{i,j}^1 - P_{\text{ref},i,j}^1)^2}{\sum_{i,j \in \text{grid}} J_{i,j} (P_{i,j}^1)^2}},$$

where $J_{i,j}$ is the Jacobian factor, and $P_{\text{ref},i,j}^1$ is the B-spline-interpolated value of the reference solution at the coarse grid node (i, j) . The results are presented in Fig. 6, and clearly demonstrate the predicted second-order scaling.

5.5. Kink ($m = 1$) instability in screw pinch in helical coordinates

This test demonstrates the ability to deal with singular coordinate configurations. We employ a force-free equilibrium in cylindrical coordinates given by [29]:

$$B_r = 0; \quad B_\theta = \frac{B\zeta}{1+\zeta^2}; \quad B_z = \sqrt{1 - B^2[1 - (1+\zeta^2)^{-2}]},$$

where $\zeta = r/\lambda$, with $\lambda = 0.5$. This equilibrium is characterized by a safety factor $q = rB_z/RB_\theta$ given by:

$$q(\zeta) = \frac{\lambda}{RB} \sqrt{(1+\zeta^2)^2(1-B^2) + B^2},$$

which is monotonically increasing (Tokamak-like) for $B < 1$, flat for $B = 1$, and monotonically decreasing (screw-pinch-like) for $B > 1$. Here, a pinch-like profile is chosen with

$$B = (\lambda^2 + a^2)/\sqrt{(\lambda^2 + a^2)^2 - \lambda^4} > 1,$$

where a is defined such that $q(a/\lambda) = 0$.

This equilibrium configuration is three-dimensional, and perturbations are of the form $\chi(r)e^{i(m\theta+kz)}$. However, one can reduce it to a two-dimensional problem by focusing on a single (m, k) mode and using a helical coordinate system [16]:

$$\xi_1 = r, \quad \xi_2 = \theta + \frac{k}{m}z, \quad \xi_3 = z.$$

In this representation, ξ_3 becomes ignorable; $\xi_3 = 0$ is chosen for convenience.

Simulations are performed with the initial value solver for a kink instability ($m = 1$), which is a stringent test of the numerical treatment of the singular point at $r = 0$. Other important parameters are: $a = \sqrt{2}$, $k = -2$, $\eta = \nu = D = 10^{-3}$, $T_0 = 10^{-5}$ (plasma beta $\beta_0 = 2p_0/B_0^2 \ll 1$), and $\gamma = 1$ (isothermal plasma). The linear eigenvalue

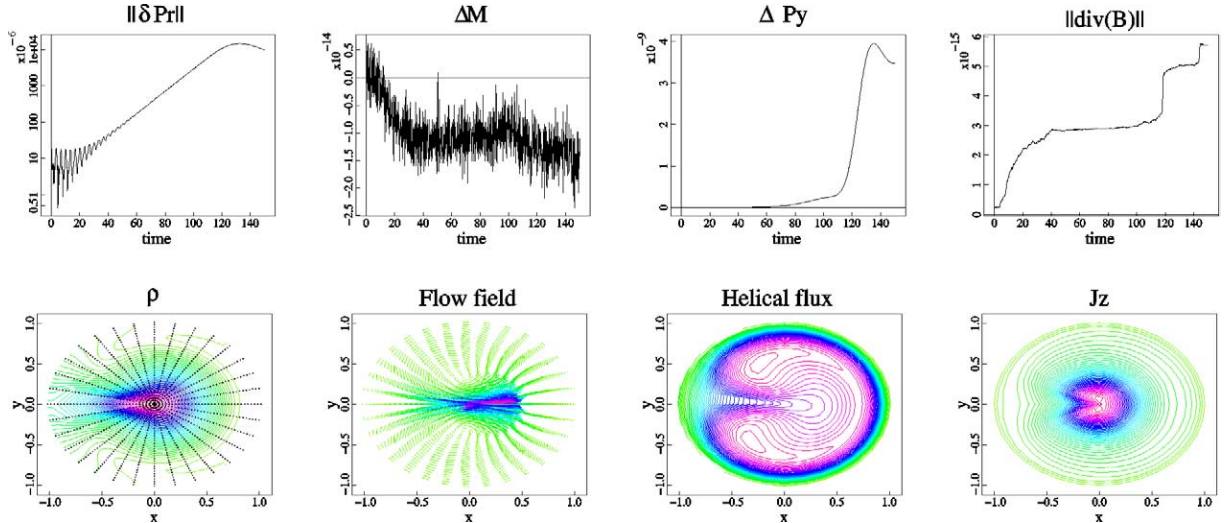


Fig. 7. Results from the simulation of the kink instability in helical coordinates. Top figures show time histories of: the Euclidean norm of δp_r , the instantaneous change in the total mass ΔM , and the instantaneous change in the total y -component of the momentum ΔP_y , and the ℓ_1 -norm of $\nabla \cdot \vec{B}$. Bottom figures show contour plots of the density (with the grid overlaid), flow field, helical magnetic flux, and perpendicular current J_z at saturation.

solver predicts a growth rate $\gamma_{EV} = 0.071$; the initial value solver finds $\gamma_{EV} = 0.071$ on both 32×32 and 64×64 grids. Nonlinear results are shown in Fig. 7, where again it can be seen that mass and the solenoidal constraint are conserved to roundoff during the simulation, and the error in the momentum component $[\Delta P_y = \sum_{i,j} dV_{i,j} (p_y - p_{y,0})_{i,j}]$, where $p_y = p_r \sin(\theta) + p_\theta \cos(\theta)$ is small. The contour plots show the helical magnetic flux $\Theta = A_z - \frac{rk}{m} A_\theta$ (with \vec{A} the magnetic vector potential) displaced laterally (as expected for a kink mode) and wrapping around itself, and the density and flow field following the magnetic evolution. The solution is clean around the singular point, demonstrating its adequate numerical treatment in our implementation.

6. Conclusions

A cell-centered finite volume scheme suitable for implicit implementations of the 3D extended MHD formalism in arbitrary curvilinear geometries has been presented. This scheme features the following properties: (1) the magnetic field and electric current are solenoidal to numerical roundoff at all times, (2) it is conservative in particles and momentum (and energy if an energy equation is chosen), (3) it is linearly stable (no checkerboard-type instabilities) and nonlinearly stable (no antidiffusion terms present in its modified equation) even in the absence of physical dissipation, and (4) it is second-order accurate (this has been demonstrated numerically).

At the heart of the scheme is the so-called ZIP scheme, proposed by Hirt [1]. This second-order scheme proposes a suitable interpolation to find fluxes at cell faces from cell-centered quantities. A modified-equation analysis has shown that ZIP does not contain potentially antidiffusive terms that would drive nonlinear instabilities. Checkerboard instabilities are avoided in ZIP by providing coupling to the variables at the cell center of interest. Further, ZIP has been shown to satisfy the chain rule numerically, which confers it some “mimetic” quality.

In addition, a novel treatment of the geometric Coriolis force terms in the momentum equation ensures the cancellation of geometric terms for constant pressure, so that in this case body forces are zero to machine accuracy. This property, which is straightforward in the continuum, is of crucial importance to minimize momentum conservation errors in curvilinear geometry due to Coriolis force terms in the discrete. We emphasize that such cancellation is facilitated by the non-staggered feature of the spatial scheme.

These properties have been demonstrated numerically with several 2D examples in very coarse (32×32) grids, featuring ideal and resistive instabilities in a variety of geometries (Cartesian, cylindrical, helical, and sinusoidal). The initial value calculations have been performed using a Crank–Nicolson scheme with an unpreconditioned Newton–Krylov implicit solver. These results demonstrate the robustness and accuracy of the scheme for implicit implementations, making it an ideal candidate for implicit, parallel, adaptive-grid implementations.

The scheme is limited in that ZIP is not TVD, and hence large flows in coarse grids and/or low dissipation regimes may result in unphysical oscillatory behavior. While implicit implementations are not generally suitable for advection-dominated and/or shock calculations [17], it is nevertheless desirable for the robustness of the difference scheme to have a monotonic advection algorithm. Further improvement of the scheme along these lines, for instance by merging ZIP with a monotonic, flexible advection scheme such as SMART [19], is left for future work.

Acknowledgements

The author acknowledges useful conversations with D.C. Barnes, D.A. Knoll, V.A. Mousseau, M. Pernice, J.M. Finn and A.H. Glasser. This research is supported by the Department of Energy, under contract W-7405-ENG-36.

Appendix A. Curvilinear components of tensor $\nabla \vec{v}$

In the development of the spatial difference scheme, we require two sets of curvilinear tensor components of $\nabla \vec{v}$: $[\nabla \vec{v}]^{ki}$, and ${}^k[\nabla \vec{v}]_i$. The curvilinear components $[\nabla \vec{v}]^{ki}$ are given by:

$$[\nabla \vec{v}]^{ki} = J^2 \vec{k} \cdot [\nabla \vec{v}] \cdot \vec{i}, \quad (\text{A.1})$$

with \vec{k} and \vec{i} normal vectors. The gradient operator reads $\nabla = \vec{l} \partial_l$, and the velocity vector reads, in the contravariant representation, $\vec{v} = v^n \underline{n}$. Introducing these into Eq. (A.1), we have:

$$[\nabla \vec{v}]^{ki} = J^2 \vec{k} \cdot [\nabla \vec{v}] \cdot \vec{i} = J g^{kl} \partial_l (v^n \underline{n}) \cdot \vec{i}.$$

Rewriting $\partial_l (v^n \underline{n}) \cdot \vec{i} = \partial_l (v^n \underline{n} \cdot \vec{i}) - v^n (\partial_l \vec{i}) \cdot \underline{n} = \partial_l (v^i / J) - v^n J \underline{l} \cdot (\nabla \vec{i}) \cdot \underline{n}$, and recalling that $\vec{i} = \nabla \xi_i$, $\Gamma_{ln}^i = -J^2 \underline{l} \cdot (\nabla \nabla \xi_i) \cdot \underline{n}$, and $\partial_l J = J \Gamma_{lk}^k$, we find:

$$[\nabla \vec{v}]^{ki} = g^{kl} (\partial_l v^i - v^i \Gamma_{ln}^n + v^n \Gamma_{ln}^i).$$

Regarding the curvilinear components $^k[\nabla \vec{v}]_i$, they are given by:

$$^k[\nabla \vec{v}]_i = J^2 \vec{k} \cdot [\nabla \vec{v}] \cdot \underline{i},$$

where \underline{i} is a tangential vector. We can readily show that:

$$^k[\nabla \vec{v}]_i = J \vec{k} \cdot [\nabla (J \vec{v} \cdot \underline{i})] - J \vec{k} \cdot \nabla (J \underline{i}) \cdot \vec{v} = J \vec{k} \cdot \nabla v_i - J \vec{k} \cdot \nabla \left(\frac{\partial \vec{x}}{\partial \xi_i} \right) \cdot \vec{v}.$$

Recalling the definition of Γ_{lm}^n in Eq. (19), we readily arrive at:

$$^k[\nabla \vec{v}]_i = g^{kl} (\partial_l v_i - \Gamma_{il}^n v_n).$$

Appendix B. No-stress boundary condition for plasma flow in general geometries

The no-stress condition enforces the cancellation of the viscous stress in the angular momentum conservation law at the boundary, thus preventing viscous decay of the angular momentum of the plasma. The angular momentum conservation law is derived from the equation of motion (Eq. (8)) by crossing it with \vec{r} , and reads:

$$\partial_t \vec{\ell} - \nabla \cdot (\vec{T} \times \vec{r}) + \rho v \nabla \times \vec{v} = \vec{0}, \quad (\text{B.1})$$

where $\vec{\ell} = \vec{r} \times \rho \vec{v}$, and $\vec{T} = \rho \vec{v} \vec{v} - \vec{B} \vec{B} + \vec{T} p_{\text{tot}} - \rho v \nabla \vec{v}$. Integrating Eq. (B.1) over an arbitrary domain Ω with surface boundary $\partial \Omega$ gives:

$$\partial_t \vec{L} - \oint_{\partial \Omega} \frac{dS}{\|\vec{n}\|} \vec{n} \cdot [\vec{T} \times \vec{r}] + \int_{\Omega} dV \rho v \nabla \times \vec{v} = \vec{0},$$

where $\vec{L} = \int_{\Omega} dV \vec{\ell}$. Isolating the viscous contribution, and neglecting density gradients, gives the *global* no-stress condition:

$$\oint_{\partial \Omega} \frac{dS}{\|\vec{n}\|} \rho v [\vec{n} \cdot (\nabla \vec{v}) \times \vec{r} + \vec{n} \times \vec{v}] = \vec{0}.$$

Since this applies to arbitrary surfaces $\delta \Omega$, it follows the *local* no-stress condition:

$$\vec{n} \cdot (\nabla \vec{v}) \times \vec{r} + \vec{n} \times \vec{v} = \vec{0}.$$

Noting that $\vec{n} \cdot (\nabla \vec{v}) \times \vec{r} = \vec{n} \cdot \nabla [\vec{v} \times \vec{r}] + \vec{n} \times \vec{v}$, the last result can be rewritten as:

$$\vec{n} \cdot \nabla [\vec{v} \times \vec{r}] + 2 \vec{n} \times \vec{v} = \vec{0}. \quad (\text{B.2})$$

In configurations where a logical coordinate is a function of r only [i.e. $\xi_n = \xi_n(r)$] (as is the case in cylindrical, toroidal, and spherical coordinate systems), we have $\vec{n} = \nabla \xi_n \parallel \vec{r}$ and Eq. (B.2) specializes to:

$$\vec{r} \cdot \nabla [\vec{v} \times \vec{r}] - 2\vec{v} \times \vec{r} = \vec{0},$$

the solution of which is $\vec{v} \times \vec{r} = \vec{\omega} r^2$, with $\vec{\omega}$ a constant tangential vector ($\vec{\omega} \cdot \vec{r} = 0$). Physically, this corresponds to free-slip angular rotation with constant angular velocity $\vec{\omega}$. This algebraic relationship can be used to fill the ghost cell values from the boundary cell values by the prescription: $[(\vec{v} \times \vec{r})/r^2]_{i+1,j} = [(\vec{v} \times \vec{r})/r^2]_{i,j}$.

In other geometries, \vec{r} generally is not parallel to \vec{n} (in fact, the origin of \vec{r} is arbitrary). It is then useful to decompose Eq. (B.2) into normal ($\vec{n} \cdot$) and tangential ($\vec{n} \times$) components, to find:

$$\begin{aligned} \vec{r} \cdot [(\vec{n} \cdot \nabla \vec{v}) \times \vec{n}] &= 0, \\ (\vec{n} \cdot \nabla \vec{v} \cdot \vec{n}) \vec{r}_t + n^2 \vec{v}_t &= \vec{0}, \end{aligned}$$

where the first condition has been used to simplify the second, and \vec{r}_t , \vec{v}_t are tangential vectors. The first relation gives a position-independent, unambiguous constraint $[(\vec{n} \cdot \nabla \vec{v}) \times \vec{n} = \vec{0}]$ that can be employed as a boundary condition in a general setting. In fact, it is a “solvability condition” (necessary but not sufficient) for the general condition in Eq. (B.2) that uniquely determines the tangential velocity components. In this light, we can regard the second relation as a constraint on \vec{r}_t , which is irrelevant.

Appendix C. Preservation of the conservation properties by the Newton–Krylov implicit algorithm

Conservation equations of the form $\partial_t U + \nabla \cdot \vec{F}(U) = 0$. Consider the conservation equation of the form:

$$\partial_t U + \nabla \cdot \vec{F}(U) = 0, \quad (\text{C.1})$$

where U is assumed here to be a scalar without loss of generality. Discretizing implicitly in time, the nonlinear system reads:

$$U^{n+1} + \theta \Delta t \nabla \cdot [\vec{F}(U^{n+1})] = \sum_{i < n+1} [\beta_i U^i + \gamma_i \Delta t \nabla \cdot \vec{F}(U^i)], \quad (\text{C.2})$$

where the superscript i samples previous time levels, and θ , β_i , γ_i are constants that depend on the details of the time difference scheme. Consistency of the time integration scheme requires $\sum_{i < n+1} \beta_i = 1$. We abbreviate Eq. (C.2) as $L(U^{n+1}) = \text{rhs}_u$. Each Newton iteration requires the solution of the linearized system:

$$\delta U_k + \theta \Delta t \nabla \cdot \left(\frac{\partial \vec{F}}{\partial U} \Big|_k \delta U_k \right) = \text{rhs}_u - L(U_k),$$

where the subscript k represents the Newton iteration level, and δU_k is the Newton update (the next Newton iterate is found as $U_{k+1} = U_k + \delta U_k$). We symbolize this equation as $(I + J_k) \delta U_k = \text{rhs}_{\delta u}$, where $J_k \delta U_k = \theta \Delta t \nabla \cdot (\frac{\partial \vec{F}}{\partial U} \Big|_k \delta U_k)$ and $\text{rhs}_{\delta u} = \text{rhs}_u - L(U_k)$.

Let us define a discrete volume integral operator $\mathcal{I}_V = \sum_{\text{grid}} \Delta V \approx \int dV$, where $\mathcal{I}_V : \mathbb{R}^N \rightarrow \mathbb{R}$, and N is the number of grid points, such that the discrete version of the divergence operator, $\mathcal{D} : \mathbb{R}^{d \times N} \rightarrow \mathbb{R}^N$ (where d is the number of spatial dimensions considered) satisfies $\mathcal{I}_V \mathcal{D} \vec{a} \equiv 0$ for an arbitrary vector $\vec{a} \in \mathbb{R}^{d \times N}$. This is a statement that the spatial difference scheme be conservative for a given discrete integral operator.

Assume that all previous time levels are conservative, i.e. $\mathcal{I}_V \vec{U}^i = C$, $\forall i < n + 1$, with $\vec{U}^i \in \mathbb{R}^N$ being the discrete representation of U at time level i . We prove next that the Newton–Krylov algorithm ensures that the next time level is conservative also, i.e. $\mathcal{I}_V \vec{U}^{n+1} = C$, regardless of the nonlinear tolerances employed. First, we note that, since the proposed spatial scheme satisfies $\mathcal{I}_V \mathcal{D} \vec{a} \equiv 0$, the following relations are true for the Newton iterate \vec{U}_k (recall that, upon convergence, $\vec{U}^{n+1} = \vec{U}_k$):

- $\mathcal{I}_V \vec{\text{rhs}}_u = \mathcal{I}_V \sum_{i < n+1} [\beta_i \vec{U}^i + \gamma_i \Delta t \mathcal{D}[\vec{F}(\vec{U}^i)]] = \sum_{i < n+1} \beta_i \mathcal{I}_V \vec{U}^i = C \sum_{i < n+1} \beta_i = C$, since $\sum_{i < n+1} \beta_i = 1$.
- $\mathcal{I}_V \mathcal{L}(\vec{U}_k) = \mathcal{I}_V [\vec{U}_k + \theta \Delta t \mathcal{D}[\vec{F}(\vec{U}_k)]] = \mathcal{I}_V \vec{U}_k$, with $\mathcal{L}(\vec{U}) : \mathbb{R}^N \rightarrow \mathbb{R}^N$ the discrete version of $L(U)$.
- $\mathcal{I}_V \mathcal{J}_k \vec{a} = \theta \Delta t \mathcal{I}_V \mathcal{D}(\frac{\partial \vec{F}}{\partial \vec{U}}|_k \vec{a}) = 0$, for arbitrary $\vec{a} \in \mathbb{R}^N$, with $\mathcal{J}_k : \mathbb{R}^N \rightarrow \mathbb{R}^N$ the discrete version of J_k .
- $\mathcal{I}_V \vec{\text{rhs}}_{\delta u} = \mathcal{I}_V [\vec{\text{rhs}}_u - \mathcal{L}(\vec{U}_k)] = C - \mathcal{I}_V \vec{U}_k$.

The Krylov algorithm inverts the Jacobian matrix $(I + \mathcal{J}_k)$ iteratively by a suitable combination of Krylov vectors, which span the Krylov subspace $\{\vec{r}_0, (I + \mathcal{J}_k)\vec{r}_0, (I + \mathcal{J}_k)^2\vec{r}_0, \dots, (I + \mathcal{J}_k)^{N-1}\vec{r}_0\}$, with N the rank of $(I + \mathcal{J}_k)$, and $\vec{r}_0 = \vec{\text{rhs}}_{\delta u}$ the initial residual [30]. Therefore, the *exact* solution $\delta \vec{U}_k$ is given by:

$$\delta \vec{U}_k = \sum_{j=0}^{N-1} \alpha_j (I + \mathcal{J}_k)^j \vec{\text{rhs}}_{\delta u} = \sum_{j=0}^{N-1} \alpha'_j \mathcal{J}_k^j \vec{\text{rhs}}_{\delta u},$$

where the α_j are coefficients found by the Krylov algorithm, and the α'_j result from the expansion of the binomial $(I + \mathcal{J}_k)^j$. The *iterative* solution $\delta \vec{U}_k^*$ at the Krylov iteration m is obtained by truncating the series at $(m - 1)$ instead of $(N - 1)$, giving:

$$\delta \vec{U}_k^* = \sum_{j=0}^{m-1} \alpha'_j \mathcal{J}_k^j \vec{\text{rhs}}_{\delta u}.$$

Integrating this result over the domain, and using the properties outlined above, there results:

$$\mathcal{I}_V \delta \vec{U}_k^* = (C - \mathcal{I}_V \vec{U}_k) \alpha'_0.$$

Since $\vec{U}_{k=0} = \vec{U}^n$, and $\mathcal{I}_V \vec{U}^n = C$ by assumption, it follows by induction that $\mathcal{I}_V \delta \vec{U}_k^* = 0$ for $k \geq 0$, and that $\mathcal{I}_V \vec{U}_k = \mathcal{I}_V (\vec{U}_{k-1} + \delta \vec{U}_{k-1}^*) = C$. This proves that the conservation property is maintained by the Newton–Krylov algorithm, regardless of nonlinear convergence tolerances.

Effect of preconditioning. We therefore conclude that finite nonlinear convergence tolerances cannot alter the conservation properties of the scheme in conservation equations of the form in Eq. (C.1) when an *unpreconditioned* Newton–Krylov algorithm is employed. However, Krylov algorithms are usually implemented with some sort of preconditioning, and hence its effects on conservation need be considered.

Krylov methods can employ right or left preconditioning. In *right preconditioning*, the Jacobian system $\mathcal{J}_k \delta \vec{x} = \vec{r}$ is rewritten as $\mathcal{J}_k P_k^{-1} \delta \vec{y} = \vec{r}$, with $\delta \vec{x} = P_k^{-1} \delta \vec{y}$, and P_k^{-1} the preconditioner. The Krylov iterative method then solves for $\delta \vec{y}$, and finds the true solution $\delta \vec{x}$ *a posteriori*. If the preconditioner inexpensively approximates the inverse of the true Jacobian, a very efficient method results. To determine the effects of right preconditioning on conservation, one simply replaces \mathcal{J}_k by $\mathcal{J}_k P_k^{-1}$ in the previous derivation to trivially show that right preconditioning has no effect on the conservation properties of the spatial scheme. At the root of this property is the fact that $\mathcal{I}_V \mathcal{J}_k P_k^{-1} \vec{a} = 0$ for arbitrary $\vec{a} \in \mathbb{R}^N$.

In *left preconditioning*, one considers the alternate equivalent Jacobian system $P_k^{-1} \mathcal{J}_k \delta \vec{x} = P_k^{-1} \vec{r}$ instead, which again could result in a very efficient solver if the preconditioner approximated the inverse of the Jacobian. However, it is not generally true that the system $P_k^{-1} \mathcal{J}_k$ satisfies $\mathcal{I}_V P_k^{-1} \mathcal{J}_k \vec{a} = 0$ for arbitrary $\vec{a} \in \mathbb{R}^N$. We therefore conclude that, in general, left preconditioning does not preserve the conservation properties of the difference scheme unless the solution is converged to machine accuracy.

Generalized conservation equations of the form $\partial_t f(U) + \nabla \cdot \vec{F}(U) = 0$. The previous discussion can be readily extended to more general conservation equations of the form $\partial_t f(U) + \nabla \cdot \vec{F}(U) = 0$, provided that the conserved

quantity f is explicitly considered as a nonlinear variable as follows:

$$\partial_t f + \nabla \cdot \vec{F}(U) = 0, \quad (\text{C.3})$$

$$f - f(U) = 0. \quad (\text{C.4})$$

The proof is similar to the previous case. Let us assume that the discrete quantity $\vec{f} \in \mathbb{R}^N$ is conserved in all previous time levels, i.e. $\mathcal{I}_V \vec{f}^i = C_f$, $\forall i < n + 1$. For the system of Eqs. (C.3) and (C.4), each Newton step k solves the following block algebraic system:

$$\begin{bmatrix} I & \mathcal{J}_k \\ I & -\partial \vec{f} / \partial \vec{U}|_k \end{bmatrix} \begin{bmatrix} \delta \vec{f}_k \\ \delta \vec{U}_k \end{bmatrix} = \begin{bmatrix} \vec{\text{rhs}}_{\delta f} \\ \vec{\text{rhs}}_{\delta u} \end{bmatrix},$$

where \mathcal{J}_k is defined as above, and $\vec{\text{rhs}}_{\delta f}$ satisfies (as shown for $\vec{\text{rhs}}_{\delta u}$ previously):

$$\mathcal{I}_V \vec{\text{rhs}}_{\delta f} = C_f - \mathcal{I}_V \vec{f}_k.$$

The Krylov iteration provides an *approximate* solution of the form:

$$\begin{bmatrix} \delta \vec{f}_k^* \\ \delta \vec{U}_k^* \end{bmatrix} = \sum_{j=0}^{m-1} \alpha_j \begin{bmatrix} I & \mathcal{J}_k \\ I & -\frac{\partial \vec{f}}{\partial \vec{U}}|_k \end{bmatrix}^j \begin{bmatrix} \vec{\text{rhs}}_{\delta f} \\ \vec{\text{rhs}}_{\delta u} \end{bmatrix} = \sum_{j=1}^{m-1} \alpha_j \begin{bmatrix} I & \mathcal{J}_k \\ I & -\frac{\partial \vec{f}}{\partial \vec{U}}|_k \end{bmatrix} \begin{bmatrix} \vec{a}_{j-1} \\ \vec{b}_{j-1} \end{bmatrix} + \alpha_0 \begin{bmatrix} \vec{\text{rhs}}_{\delta f} \\ \vec{\text{rhs}}_{\delta u} \end{bmatrix},$$

where:

$$\begin{bmatrix} \vec{a}_{j-1} \\ \vec{b}_{j-1} \end{bmatrix} = \begin{bmatrix} I & \mathcal{J}_k \\ I & -\frac{\partial \vec{f}}{\partial \vec{U}}|_k \end{bmatrix} \begin{bmatrix} \vec{a}_{j-2} \\ \vec{b}_{j-2} \end{bmatrix} = \begin{bmatrix} I & \mathcal{J}_k \\ I & -\frac{\partial \vec{f}}{\partial \vec{U}}|_k \end{bmatrix}^{j-1} \begin{bmatrix} \vec{\text{rhs}}_{\delta f} \\ \vec{\text{rhs}}_{\delta u} \end{bmatrix}, \quad (\text{C.5})$$

and $\vec{a}_0 = \vec{\text{rhs}}_{\delta f}$, $\vec{b}_0 = \vec{\text{rhs}}_{\delta u}$. Focusing on $\delta \vec{f}_k^*$ (which updates the conserved quantity), we find:

$$\delta \vec{f}_k^* = \sum_{j=1}^{m-1} \alpha_j (\vec{a}_{j-1} + \mathcal{J}_k \vec{b}_{j-1}) + \alpha_0 \vec{\text{rhs}}_{\delta f}.$$

Integrating over the domain volume we find:

$$\mathcal{I}_V \delta \vec{f}_k^* = \sum_{j=1}^{m-1} \alpha_j \mathcal{I}_V \vec{a}_{j-1} + \alpha_0 [C_f - \mathcal{I}_V \vec{f}_k].$$

Noting that, by Eq. (C.5), $\vec{a}_{j-1} = \vec{a}_{j-2} + \mathcal{J}_k \vec{b}_{j-2}$, we find that:

$$\mathcal{I}_V \vec{a}_{j-1} = \mathcal{I}_V \vec{a}_{j-2} = \dots = \mathcal{I}_V \vec{\text{rhs}}_{\delta f} = C_f - \mathcal{I}_V \vec{f}_k,$$

and hence:

$$\mathcal{I}_V \delta \vec{f}_k^* = [C_f - \mathcal{I}_V \vec{f}_k] \sum_{j=0}^{m-1} \alpha_j.$$

From this result, it follows by induction (since $\mathcal{I}_V \vec{f}_{k=0} = \mathcal{I}_V \vec{f}^n = C_f$ by assumption) that $\mathcal{I}_V \delta \vec{f}_k^* = 0$ for $k \geq 0$, thus proving conservation for arbitrary nonlinear tolerances.

One can easily show that the proof does not carry over if the compact system $\partial_t f(U) + \nabla \cdot \vec{F}(U) = 0$ is considered instead, and in this case solving to machine accuracy is required for conservation. While the alternate system in Eqs. (C.3) and (C.4) requires more computer resources per nonlinear iteration than the compact form, it is likely that, for systems where exact conservation is of the essence, it results in significant CPU savings by avoiding the need to converge the nonlinear system to machine accuracy.

References

- [1] C.W. Hirt, Heuristic stability theory for finite-difference equations, *J. Comput. Phys.* 2 (1968) 339–355.
- [2] R.J. LeVeque, *Numerical Methods for Conservation Laws*, Birkhäuser Verlag, Basel, Switzerland, 1992.
- [3] J.U. Brackbill, D.C. Barnes, The effect of nonzero $\nabla \cdot \mathbf{B}$ on the numerical solution of the magnetohydrodynamic equations, *J. Comput. Phys.* 35 (3) (1980) 426–430.
- [4] I. Lindemuth, J. Killeen, Alternating direction implicit techniques for two-dimensional magnetohydrodynamic calculations, *J. Comput. Phys.* 13 (1973) 181–208.
- [5] C.H. Finan, J. Killeen, Solution of the time-dependent, three-dimensional resistive magnetohydrodynamic equations, *Comput. Phys. Comm.* 24 (1981) 441–463.
- [6] D.D. Schnack, D.C. Barnes, D.S. Harned, E.J. Caramana, Semi-implicit magnetohydrodynamic calculations, *J. Comput. Phys.* 70 (1987) 330–354.
- [7] T. Amari, J.F. Luciani, P. Joly, A preconditioned semi-implicit method for magnetohydrodynamics equations, *SIAM J. Sci. Comput.* 21 (3) (1999) 970–986.
- [8] C.R. Sovinec, A.H. Glasser, T.A. Gianakon, D.C. Barnes, R.A. Nebel, S.E. Kruger, D.D. Schnack, S.J. Plimpton, A. Tarditi, M.S. Chu, the NIMROD team, Nonlinear magnetohydrodynamics simulation using high-order finite elements, *J. Comput. Phys.* 195 (1) (2004) 355–386.
- [9] M. Shashkov, S. Steinberg, *Conservative Finite-Difference Methods on General Grids*, Symbolic and Numeric Computation Series, CRC Press, Boca Raton, 1996.
- [10] W. Dai, P.R. Woodward, On the divergence-free condition and conservation laws in numerical simulations for supersonic magnetohydrodynamic flows, *Astrophys. J.* 494 (1998) 317.
- [11] W. Dai, P.R. Woodward, A simple finite difference scheme for multidimensional magnetohydrodynamic equations, *J. Comput. Phys.* 142 (1998) 331.
- [12] D. Ryu, F. Miniati, T.W. Jones, A. Frank, A divergence-free upwind code for multi-dimensional magnetohydrodynamics flows, *Astrophys. J.* 509 (1998) 244.
- [13] D.S. Balsara, D.S. Spicer, A staggered mesh algorithm using high order Godunov fluxes to ensure solenoidal magnetic fields in magnetohydrodynamics simulations, *J. Comput. Phys.* 149 (1999) 270–292.
- [14] D.S. Balsara, Divergence-free adaptive mesh refinement for magnetohydrodynamics, *J. Comput. Phys.* 174 (2001) 614–648.
- [15] G. Tóth, The $\nabla \cdot \mathbf{B} = 0$ constraint in shock-capturing magnetohydrodynamics codes, *J. Comput. Phys.* 161 (2000) 605–652.
- [16] D. Schnack, J. Killeen, Nonlinear, two-dimensional magnetohydrodynamic calculations, *J. Comput. Phys.* 35 (1980) 110–145.
- [17] O.S. Jones, U. Shumlak, D.S. Eberhardt, An implicit scheme for nonideal magnetohydrodynamics, *J. Comput. Phys.* 130 (1997) 231–242.
- [18] M. Wilcoxson, V. Manousiouthakis, On an implicit ENO scheme, *J. Comput. Phys.* 115 (1994) 376–389.
- [19] P.H. Gaskell, A.K.C. Lau, Curvature-compensated convective transport: SMART, a new boundedness-preserving transport algorithm, *Internat. J. Numer. Methods Fluids* 8 (1988) 617–641.
- [20] V.D. Liseikin, *Grid Generation Methods*, Springer, Berlin, New York, 1999.
- [21] R.B. Lowrie, A comparison of implicit time integration methods for nonlinear relaxation and diffusion, *J. Comput. Phys.* 196 (2) (2004) 566–590.
- [22] S.V. Patankar, *Numerical Heat Transfer and Fluid Flow*, Taylor & Francis, 1980.
- [23] J.C. Tannehill, D.A. Anderson, R.H. Pletcher, *Computational Fluid Mechanics and Heat Transfer*, second ed., Taylor & Francis, 1997.
- [24] P. Ricci, G. Lapenta, J.U. Brackbill, A simplified Maxwell solver, *J. Comput. Phys.* 183 (2002) 117–141.
- [25] S.I. Braginskii, Transport processes in a plasma, in: M.A. Leontovich (Ed.), *Reviews of Plasma Physics*, vol. 1, Consultants Bureau, New York, 1965, pp. 205–311.
- [26] J.D. Huba, *NRL plasma formulary*, NRL/PU/6790-98-358, Naval Research Laboratory, Washington, DC, 1998.
- [27] L. Chacón, D.A. Knoll, J.M. Finn, Implicit, nonlinear reduced resistive MHD nonlinear solver, *J. Comput. Phys.* 178 (1) (2002) 15–36.
- [28] L. Chacón, D.A. Knoll, A 2D high- β Hall MHD implicit nonlinear solver, *J. Comput. Phys.* 188 (2) (2003) 573–592.
- [29] H.P. Furth, P.H. Rutherford, H. Selberg, Tearing mode in the cylindrical tokamak, *Phys. Fluids* 16 (7) (1973) 1054–1063.
- [30] C.T. Kelley, *Iterative Methods for Linear and Nonlinear Equations*, SIAM, Philadelphia, 1995.